ELSEVIER

Contents lists available at ScienceDirect

Journal of Materials Research and Technology

journal homepage: www.elsevier.com/locate/jmrt





Enhanced dynamic-mechanical property and microstructural mechanism of a FeCoNiCrMo_{0.2} high-entropy alloy fabricated using powder bed fusion

Wenshu Li ^{a,b}, Ruoyu Liu ^{a,b}, Shaohong Wei ^{a,c}, Yiyu Huang ^{a,b}, Qi Wu ^{a,b}, Ao Fu ^b, Yubin Ke ^{c,d}, Peter K. Liaw ^e, Bin Liu ^b, Bingfeng Wang ^{a,b,*}

- ^a School of Materials Science and Engineering, Central South University, Changsha 410083, China
- ^b State Key Laboratory of Powder Metallurgy, Central South University, Changsha 410083, China
- Spallation Neutron Source Science Center (SNSC), Dongguan 523808, China
- ^d Institute of High Energy Physics, Chinese Academy of Sciences, Beijing 10049, China
- ^e Department of Materials Science and Engineering, The University of Tennessee, Knoxville, TN 37996, USA

ARTICLE INFO

Keywords: High-entropy alloy Powder bed fusion Mechanical property Microstructure Precipitates

ABSTRACT

Powder bed fusion (PBF), along with subsequent heat treatment, plays a crucial role in enhancing the impact toughness of FeCoNiCrMo_{0,2} high-entropy alloys (HEAs) and expanding their potential applications in field for high-speed deformation. In this study, the dynamic-mechanical properties and microstructure of the as-built PBF-FeCoNiCrMo_{0.2} HEAs and quenched PBF-FeCoNiCrMo_{0.2} HEAs heated at 600-750 °C for 8 h were investigated. As the heating temperature increases, the columnar grains and cellular structures undergo coarsening and the dislocation density gradually decreases. Moreover, higher heating temperatures facilitate the precipitation of Mo-rich second phases. This occurrence can be primarily attributed to the segregation of Mo at the boundaries of the as-built specimens. Consequently, in the quenched specimens, the µ phases are predominantly distributed along the boundaries of the cellular structures. In the quenched Q700 specimen (heated at 700 °C for 8h), the size and volume fraction of the μ phases are measured to be 63.4 nm and 3.59%, respectively. Additionally, under the same condition, the Q700 specimens also exhibited a relatively slight increase in the size of the cellular structures. The impact energy absorption, dynamic yield strength, and dynamic compressive strength of the O700 quenched specimens were found to be 210.1 MJ/m³, 1066 MPa, and 1649 MPa at a strain rate of 1840 s⁻¹. These values represent a dramatic improvement of 38.1%, 52.7%, and 14.7% higher in comparison to those of the as-built specimens. Under impact deformation, the presence of the μ phases plays a significant role in impeding the movement of dislocations by acting as a pinning agent for the boundaries of the cellular structures, thereby enhancing the strength. Simultaneously, the cellular structures were significantly elongated to form the deformation bands and to coordinate the impact deformation, leading to good impact energy absorption. In combination, the synergistic strengthening and toughening effect of the μ phases and the elongated cellular structures contribute to a remarkable improvement in the impact toughness of the PBF-HEAs.

1. Introduction

The FeCoNiCrMo $_{0.2}$ high-entropy alloy (HEA) is designed by replacing element in FeCoNiCrMn Cantor HEAs. There are σ or μ phases precipitated in the face-centered-cubic (FCC) matrix by addition of Mo, thereby achieving high strength-plasticity performance [1–3]. The powder bed fusion (PBF) technology, specifically selective laser melting (SLM), could be used to fabricate FeCoNiCrMo HEAs parts with complex shapes and good mechanical properties [4–8]. However, SLM

technology often requires the subsequent implementation such as heat treatment to alleviate the thermal stress. These process would lead to the microstructure evolution including grain coarsening and precipitation [9]. The combination of the SLM technology and subsequent implementation offers an innovative approach to designing the nanoscale microstructure in the FeCoNiCrMo $_{0.2}$ HEAs [10,11]. It is possible to further enhancing of the mechanical properties of the FeCoNiCrMo $_{0.2}$ HEAs parts and making them suitable for high-speed deformation fields such as turbine blades, aircraft landing gears, and unmanned aerial

^{*} Corresponding author. School of Materials Science and Engineering, Central South University, Changsha 410083, China. *E-mail address:* wangbingfeng@csu.edu.cn (B. Wang).

vehicles [9,12].

The fine cellular structures in the selective-laser-melted HEAs (SLM-HEAs) contribute to their exceptional mechanical properties by their small size with high dislocation density at the boundary [13,14]. Kong et al. [15] reviewed the kinetics of the size and morphology and formation mechanism, including elemental segregation and dislocation, of the cellular structures in various AM alloys and confirmed their advantageous effects on the mechanical properties of AM parts. However, these cellular structures tend to coarsen and dislocation density decreases during the post-printing heat treatment, which weakens the grain-boundary strengthening and dislocation strengthening in the SLM-HEAs. Tong et al. [16] studied the evolution of the cellular structures in the SLM-FeCoNiCrMn HEAs and found that the cellular structures exhibit great thermal stability at 500 °C but gradually transformed into recrystallized structures as the annealing temperature increased. Kuzminova et al. [17] also found that the recrystallization occurred in the SLM-FeCoNiCr HEAs when the annealing temperature exceeds 700 °C. Furthermore, it has been reported that the yield strength and the microhardness of the heat-treated SLM-HEAs decrease due to the grain coarsening during the subsequent implementation [16–19]. Hence, studying the evolution of microstructure within the cellular structure during subsequent implementation becomes crucial, enabling effective control over the coarsening process of cellular structures.

The position, fraction, shape, and size of the precipitates in SLM-HEAs play a vital role in their precipitation strengthening [20,21]. Consequently, it becomes crucial to strategically design precipitates in SLM-HEAs through additive manufacturing and subsequent implementation to achieve the desired performance. Shen et al. [22] examined the microstructure evolution of the SLM-AlCoCrFeNi HEA after annealing and found that the enhanced hardness, yield strength, and ultimate tensile strength are attributed to the precipitation of the Cr-rich σ precipitates in the B₂ matrix and precipitation of the nano-ordered L₁₂ precipitates in the FCC matrix. Similarly, Lin et al. [23] found the development of the L₁₂ precipitates within the matrix and the precipitation of the L₂₁ precipitates at the boundary of the cellular structures in the SLM-AlCoCrFeNiTi HEA after annealing at 750 °C. These result in a significant improvement in the tensile strength (~1235 MPa) and yield strength (~1550 MPa) of the SLM-AlCoCrFeNiTi HEA. Fujieda et al. [24] investigated the influence of the solution treatment on the microstructure of the selective electron beam melted CoCrFeNiTiMo HEA. They found an improvement in the tensile properties caused by the uniformly distributed precipitates with a diameter of 40 nm formed during the 1100 °C heat treatment. Peng et al. [18] found that the hardness and wear resistance of the laser-melt-deposited Al_{0.3}CoCrFeNi HEA could be improved by the generation of the B2 precipitates and the σ precipitates at the boundary of the cellular structures after annealing at 650 °C for 5h. Thapliyal et al. [25] introduced B₄C into the FeMn-CoCrSi HEA through laser additive manufacturing and achieved the segregation of B and C elements at the boundary of the cellular structures by post-annealing. The segregation of these two elements further causes the enrichment of the Cr at the boundary of the cellular structure, forming the precipitation of cubic-crystal-structured Cr2B precipitates

and hexagonal-crystal-structured Cr₇C₃ precipitates to strengthen the boundary of the cellular structures. Li et al. [26] prepared the NbC-added CoCrFeMnNi HEAs by laser beam powder bed fusion. After 800 heat treatment, these HEAs achieved superior thermal stability due to the formation of NbC precipitates at boundaries of the cellular structures, leading to high yield strength (~870 MPa). Kong et al. [27] investigates effect of heat treatment on the microstructure and mechanical properties of AlCoCrFeMnNi HEAs prepared by laser powder bed fusion. The yield strength of HEA reaches 1000 MPa after 850 $^{\circ}\text{C}$ heat treatment due to the massive BCC phases generate at the boundary of the grain and cellular structure. Table 1 summaries the post-processing, type of precipitates, and mechanical properties of HEAs in the above researches. Hence, the precipitates at the boundary of cellular structure can significantly affect the mechanical properties of the AM-HEAs. Existing reports indicate that the element segregation at the boundary of cellular structures appears in the as-built SLM-HEAs [26-29], which determines the distribution and fraction of precipitation. Therefore, the key factor in improving the mechanical properties of the SLM-FeCoNiCrMo_{0,2} HEAs lies in designing element segregation on the boundary of the cellular structures and controlling precipitate formation by additive manufacturing and subsequent implementation.

Dynamic-mechanical property is an important indicator for evaluating whether metallic materials could be used under high strain-rate impact deformation, among which the impact toughness represents the ability to absorb impact energy [30]. Attaining exceptional impact toughness requires materials to possess high strength and ductility [31]. High strength allows a material to resist impact deformation and withstand external forces, while good ductility enables the material to undergo plastic deformation and absorb energy during impact events [32]. The synergy between strength and ductility is the key to enhancing impact toughness. It can effectively absorb and distribute impact forces, thereby enhancing its overall toughness in demanding applications [33]. In our previous work [34], we have reported a significant strength improvement in the SLM-HEAs heated at 800 $^{\circ}$ C. The key to this research to this strength enhancement lies in the molt pool regulation and precipitation strengthening. The disappearance of the cellular structure and the significant coarsening of grain size at high heating temperatures have led to a decrease in ductility, resulting in a slightly reduced impact toughness.

Dynamic-mechanical property is an important indicator for evaluating whether metallic materials could be used under high strain-rate impact deformation, among which the impact toughness represents the ability to absorb impact energy [30]. Attaining exceptional impact toughness requires materials to possess high strength and ductility [31]. High strength allows a material to resist impact deformation and withstand external forces, while good ductility enables the material to undergo plastic deformation and absorb energy during impact events [32]. The synergy between strength and ductility is the key to enhancing impact toughness. It can effectively absorb and distribute impact forces, thereby enhancing its overall toughness in demanding applications [33]. In our previous work [34], we have reported a significant strength improvement in the SLM-HEAs heated at 800 °C. The key to this research

Table 1
Chemical composition, additive manufacturing method, post-processing, type of precipitates and mechanical property of HEAs in references [22–27].

AM	Post-processing	Type of precipitates	Mechanical property	Reference
SLM	600 °C/8h	σ phase, B ₂ phase	YS: 810 MPa	[22]
			UTS: 1115 MPa	
SLM	750 °C/50h	L_{12} , L_{21} phase	YS: 1235 MPa	[23]
			UTS: 1550 MPa	
SEBM	1100 °C/50h	Ni ₃ Ti phase	YS: 815 MPa	[24]
			UTS: 1050 MPa	
L-PBF	900 °C/10min	Cr ₂ B, Cr ₇ C ₃ phase	UTS: 1180 MPa	[25]
		- ' ' ' '	EL: 17%	
L-PBF	800 °C/2h	NbC phase	YS: 870 MPa	[26]
L-PBF	850 °C/5h	NiAl phase, σ phase	YS: 1000 MPa	[27]
	SLM SEBM L-PBF L-PBF	SLM 600 °C/8h SLM 750 °C/50h SEBM 1100 °C/50h L-PBF 900 °C/10min L-PBF 800 °C/2h	$\begin{array}{cccccccccccccccccccccccccccccccccccc$	$\begin{array}{cccccccccccccccccccccccccccccccccccc$

to this strength enhancement lies in the molt pool regulation and precipitation strengthening. The disappearance of the cellular structure and the significant coarsening of grain size at high heating temperatures have led to a decrease in ductility, resulting in a slightly reduced impact toughness.

The aim of this study is to investigate the simultaneous precipitation of second phase with controlling the coarsening of the cellular structures by SLM and subsequent heating and quenching process, thereby achieving strength-plasticity balance and improving the impact toughness. The deformation mechanisms of the second-phase and cellular structure during the impact deformation, as well as their contributions to the strengthening mechanisms are discussed.

2. Materials and methods

Fig. 1 shows the preparation process and dynamic-mechanical property testing method of the materials in this work. Fig. 1(a) illustrates the pre-alloyed powder used in this study, with its chemical composition presented in Table 2 [35]. The size distribution of the pre-alloyed powder is counted in Fig. 1(b), with an average size of approximately 67.1 μm [35]. The preparation method for the pre-alloyed powder involved initially melting pure metal powders in a vacuum induction furnace to form pre-alloyed ingots. Subsequently, the pre-alloyed ingots were subjected to high-speed airstream in an atomization chamber, resulting in their fragmentation into small droplets that solidified to form fine powder. The powder morphology is approximately spherical, with a small quantity of satellite particles.

Fig. 1(c) presents a schematic diagram of the SLM preparation process. The SLM procedure was carried out using FS301 M system (Farsoon technologies, P. R. China) within an Ar atmosphere protection. A rectangular specimen measuring 10 \times 10 \times 70 mm was fabricated. Subsequently, a series of $\Phi6 \times 7.2$ mm cylindrical specimens were machined along the scanning direction on the rectangular specimen. Fig. 1(d) illustrates the schematic diagram depicting the preparation process employed in this investigation. As per our previous work [35], three sets of printing parameters were used in the SLM process, and the dynamic-mechanical properties of the as-built specimens could be improved by the control of the printing parameters. Among the various options, the specimen 2, created using printing parameters of 330 W power and 800 mm/s scanning speed, exhibited outstanding performance (The impact toughness and yield strength reach 315.6 MJ/m³ and 775.6 MPa at a strain rate of 2420 s^{-1}). So the specimen 2 with the same printing parameters was chosen for the subsequent heating and quenching. It is essential to note that the fabrication method of cylindrical specimens in this study differs from that in our previous work [35], with the loading direction of the cylindrical specimens being aligned with SLM scanning direction. The shift of the loading direction is attributed to the anisotropic mechanical performance SLM-specimens, and property along the scanning direction is superior than that along the building direction. The dynamic mechanical properties of the as-built specimens along the different loading direction are given in Appendix C. Before heating, the cylindrical specimens were placed inside a vacuum glass tube. Then, the vacuum tube was purged with argon gas for a minimum of three cycles to remove any residual air inside the glass tube. Later, the glass tubes containing the specimens underwent a high-temperature sintering process for 10 min to ensure an airtight seal, thus providing an inert gas protective environment during the heating process. The treatment was carried out at temperatures of 600, 650, 700, and 750 °C with specimens labeled as Q600, Q650, Q700, and Q750, respectively, using the DZSX2-10-12NP (Yun Yue, P. R. China). These specimens were heated for 8 h, then quenched with industrial oil to prevent the growth of grains and second phases. The specific SLM process parameters along with the subsequent heating parameters are listed in Table 3.

Dynamic-mechanical properties of the SLM-FeCoNiCrMo $_{0,2}$ HEAs were tested using a split Hopkinson pressure bar. The schematic diagram

is shown in Fig. 1(e). The cylindrical specimen was placed between the incident bar and transmitter bar, ensuring alignment along their central axes. The impact force of the strike bar was provided by a vacuum gas charging system. Subsequently, the strike bar was propelled to strike the incident bar, specimen, and transmitter bar. Strain gages affixed to the incident bar and transmitter bar were used to collect strain signals, which were then processed to obtain values for engineering stress, engineering strain, true stress, true strain and strain rate. Detailed calculations are provided in Appendix A. The actual dimensions, deformation parameters and conditions of different specimens are given in Table 4.

To identify the phases of the SLM-FeCoNiCrMo $_{0.2}$ HEAs, X-ray diffraction (XRD) was conducted using an Empyrean diffraction instrument (PANalytical, Netherlands) with an incident beam of the Cu-K α radiation at 50 kV. Scanning was performed over a range of 10° – 90° at a rate of 2° /min. The microstructural characterizations of various specimens were conducted using optical microscopy (DM2700 M, Leica, Germany), scanning electron microscope (Quanta-250, FEI, Netherlands, operating voltage: 30 KV), transmission electron microscopy (Tecnai G20, FEI, U.S.A. operating voltage: 250 KV), respectively. An Image-pro plus (IPP) image analysis software was used to analyzed the size of the cellular structures [35]. The size and fraction of the phases are determined using small angle neutron scattering (SANS) technique. By employing an incident neutron wavelength ranging from 1 to $10~\text{Å}^{-1}$, the scattering intensity was collected in the range from 0.005 Å $^{-1}$ to 0.2 Å $^{-1}$ as a function of the scattering vector, Q.

3. Results

3.1. Dynamic mechanical property of SLM-FeCoNiCrMo_{0.2} HEAs

The dynamic mechanical properties of the as-built specimen and quenched specimens are presented in Fig. 2.

The engineering stress vs. engineering strain curves of the SLM-FeCoNiCrMo_{0.2} HEAs deformed with the average velocity of the strike bar of 20 m/s are shown in Fig. 2(a). It can be observed that under the same impact condition, the maximum engineering strain of the as-built specimen is higher than that of the quenched specimens, whereas the flow stress of the quenched specimens is higher than that of the as-built specimens. The true stress and true strain in the as-built specimen and quenched specimens are obtained by converting engineering stress and engineering strain, respectively. The true stress vs. true strain curves displayed in Fig. 2(b) exhibit a similar trend to the engineering stress vs. engineering strain curves. The yield strength and ultimate compressive strength of as-built specimen and quenched specimens are determined using engineering stress vs. engineering strain curves. Additionally, the impact toughness of as-built specimen and quenched specimens are quantified as impact energy by calculating the area of the true stress vs. true strain curves. Fig. 2(c) depicts a comparative assessment of these values. The yield strength, ultimate compressive strength and impact energy of the as-built specimen are 698 \pm 38 MPa, 1407 \pm 59 MPa and 159 ± 5.3 MJ/m³. There is a general trend of increasing yield strength, ultimate compressive strength and impact energy as moving from the asbuilt specimen to the quenched specimens. Notably, yield strength, ultimate compressive strength and impact energy of the Q700 specimen reach peak values of approximately 1066 \pm 42 MPa, 1649 \pm 46 MPa, and 214.5 \pm 6.5 MJ/m³ respectively. These values represent significant improvement of 52.7%, 17.2% and 34.9% compared to those of the asbuilt specimen, respectively. However, the Q750 specimen experiences a slight decline in yield strength compared to the Q700 specimen, while its strength (yield strength 1005 ± 28 MPa, ultimate compressive strength 1605 \pm 78 MPa) and impact toughness (impact energy 196.4 \pm 4.5 MJ/m³) remains relatively high. Furthermore, direct comparison of the dynamic mechanical properties of the SLM-FeCoNiCrMo_{0.2} HEAs with other materials is given in Fig. 2(d), including HEAs [36–40], steels [41-43], Ni-based alloy [44], and Al-based alloys [45-47]. It is clear that the Q700 specimen in this work demonstrate excellent

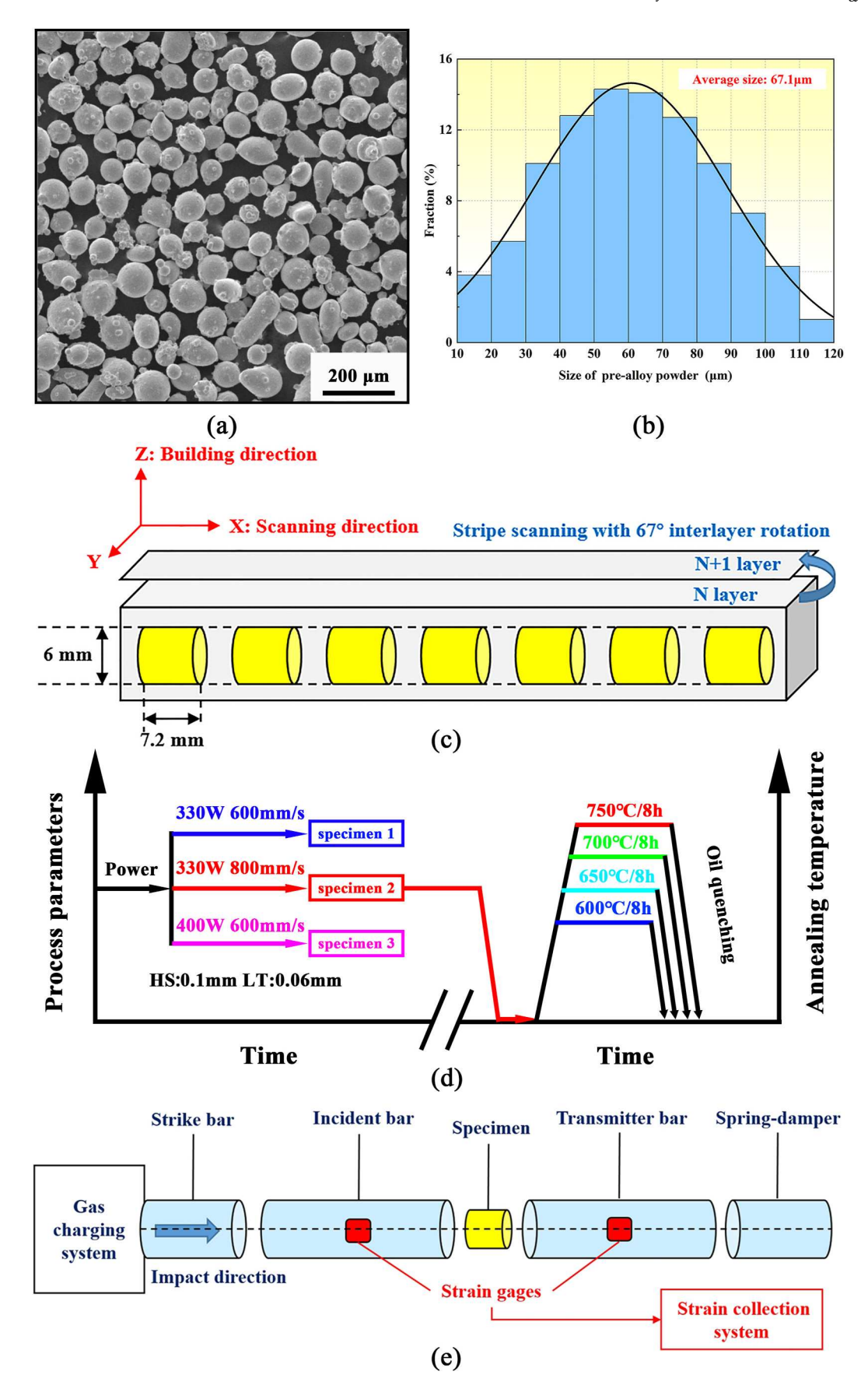


Fig. 1. Schematic diagram of the preparation process and dynamic-mechanical property testing method. (a) Morphology of pre-alloyed powder. (b) Size distribution diagram of pre-alloy powder. (c) Schematic diagram of SLM process. (d) Process parameters of SLM and heat treatment. (e) Schematic diagram of split Hopkinson pressure bar [35].

Table 2Composition of the FeCoNiCrMo_{0.2} pre-alloyed powder [35].

Element	Fe	Co	Ni	Cr	Мо
Component (at. %)	21.13	24.5	23.67	24.51	4.61

strength-impact toughness combinations that surpass those of other alloys.

3.2. Microstructure of SLM-FeCoNiCrMo_{0,2} HEAs

Fig. 3 illustrates the XRD patterns of the as-built specimen and quenched specimens at various heating temperatures [35]. It is evident that the as-built specimen is composed of a single FCC phase, with the diffraction peak of the μ phase observed in the Q700 specimen and Q750 specimen. The formation of σ phase during higher heating temperature has been reported in our earlier work [34]. According to the researches on the FeCoNiCrMox HEAs system [1,48], the disparity in precipitation conditions between the μ phase and σ phase is relatively minimal. Typically, an increasing Mo content is correlated with a greater propensity for μ phase formation. The precipitation behaviors of both μ phase and σ phase will be discussed later.

Fig. 4 presents the microstructure of the as-built specimen [35]. In Fig. 4(a)—a three-dimensional optical image reveals the distinct features of the melt pools observed in the as-built specimen. The morphology of these molt pools resembles overlapping semi-elliptical cylinders. Fig. 4 (b) exhibits the fine cellular structures within the molten pools, boasting an average size of approximately 486.3 nm. Notably, a TEM image of the cellular structures suggests that their boundary consist of high density dislocations, as shown in Fig. 4(c). Additionally, Fig. 4(d) displays an element distribution of the cellular structures, where there is Mo segregation at the boundary of the cellular structure. It is worth mentioning that few precipitates could be observed in the as-built specimen.

The heating and quenching process lead to the microstructural evolution of melt pool and grain in the as-built specimen. According to Fig. 1(c) and (e), the dynamic loading direction of the cylindrical specimens are consistent with the scanning direction. To investigate the relation between the dynamic mechanical property and the corresponding microstructure, the microstructure along the scanning direction (X direction in Fig. 1(c)) is characterized. Fig. 5 presents the microstructure of melt pool and columnar grain in the quenched specimens with different heating temperatures. In comparison to the as-built specimen, there is no obvious change in the melt pool in the Q600 specimen. As the heating temperature increased, the columnar grains within the melt pool became more prominent and the boundaries became gradually clearer. In the Q750 specimen, the boundaries of the melt pool tend to blur. This aligns with the observed trend in our previously published results [34]. It is noted that the boundaries of melt pool essentially vanished at heating temperatures exceeding 800 °C, leaving columnar grains as the predominant microstructure [34].

The microstructure evolution and size distribution of the cellular structures in the quenched specimens are depicted in Fig. 6. The cellular structures in the as-built specimen present the hexagonal-equiaxed morphology, as presented in Fig. 6(a1). Notably, there is a significant variation in the size of the cellular structures. As the heating

 Table 4

 Dimensions and deformation conditions of cylindrical specimens.

Specimens ID	Diameter (mm)	Height (mm)	Velocity of strike bar (m/s)	Average strain rate (s^{-1})
As built	6.03	6.83	19.56	1840
Q600	5.97	6.81	19.79	1800
Q650	6.11	6.83	20.14	1860
Q700	5.92	6.84	20.41	1830
Q750	5.98	6.79	20.24	1830

temperature rises, the sizes of the cellular structures show an upward trend, as demonstrated in Fig. 6(b1) and (c1). However, in the Q700 specimen and Q750 specimen, the boundaries of cellular structures disappear, resulting in no further increase in the average size of cellular structures for these two specimens, represented in Fig. 6(d1) and (f1). The size distributions and corresponding average sizes of the cellular structures in various quenched specimens are presented in Fig. 6(a2). The average size of the cellular structures in as-built specimens is measured to be 486.3 \pm 123.9 nm, while in Q650 specimen it reaches a maximum value of 966.1 \pm 257.8 nm, which is 100.6 % higher than that in the as-built specimen, as exhibited in Fig. 6(b2) and 6(c2). The average sizes of cellular structures in Q700 specimen and Q750 specimen are approximately 904.4 nm and 880.4 nm, respectively. Once the heating temperature surpasses 800 °C, the cellular structure within the melt pool largely vanishes [34]. Moreover, a number of precipitates, identified as μ phases based on the XRD result, were observed at the boundary of cellular structures in the Q700 specimen and Q750 specimen, as shown in Fig. 7. There are two types of μ phases within the specimens, positioned at different locations. One is located at the boundary of the cellular structures, as indicated by the blue dashed line box, shown in Fig. 7(a). The other is situated at the boundary of the melt pool, identified by the yellow dashed line box, shown in Fig. 7(b).

Further bright-field images in Fig. 8(a) reveals intricate details regarding the microstructure of the cellluar structure and μ phases in the Q700 specimen. It is demonstrated that the μ phases exhibit a rod-like shape and are predominantly distributed along the boundary of the cellular structures. Fig. 4(c) illustrates that the boundaries of cellular structures in the as-built specimens contain a high-density dislocations. However, upon heating and quenching, a notable reduction in the dislocation density at these boundaries is observed. Cellular structures exist in the form of dislocation cells. After heat treatment, the dislocations at the boundaries of cellular structures move and annul each other due to thermal driving forces, resulting in a decrease in dislocation density. Simultaneously, the gradual annihilation of boundaries causes an increase in the size of cellular structures. With an increase in heat treatment temperature, the interaction between dislocations is intensified, resulting in a further decrease in dislocation density and an increase in the size of the cellular. The high-angle annular dark-field scanning-TEM (HAADF-STEM) image and corresponding EDS map in Fig. 8(b) further confirm that the μ phase correspond to Mo-rich precipitates. Fig. 8(c) shows the high-resolution TEM images, while Fig. 8 (d) displays the corresponding FFT pattern of μ phase in the Q700 specimen obtained via a Fast Fourier transform in Fig. 8(c). Notably, two sets of SAED patterns are evident, representing an FCC phase along a <110> zone axis, and a hexagonal-close-packed (HCP) phase along a <1210> zone axis, denoting the crystal structures of the matrix and the

Table 3Selective laser melting process parameters and heat treatment parameters of cylindrical specimens.

Specimens ID	Process parameters of SLM	Densification (%)	Heating Temperature (°C)	Holding Time (h)	Quenching
As built	Laser power: 330 W	99.11	_	8	Oil quenching
Q600	Scan speed: 800 mm/s	99.39	600		
Q650	Layer thickness: 0.06 mm	99.26	650		
Q700	Hatch distance: 0.1 mm	99.13	700		
Q750	Stripes with 67° rotation	98.97	750		

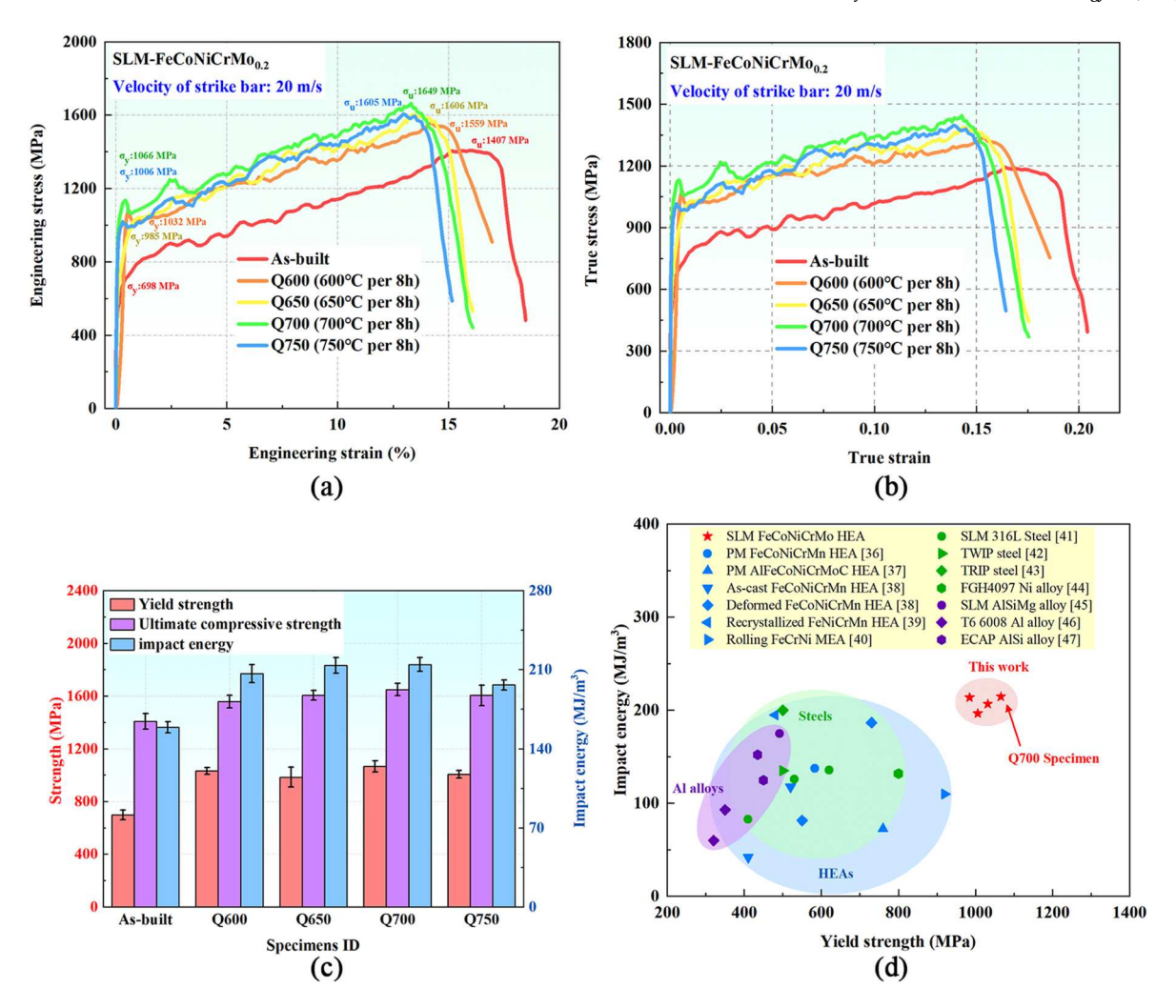


Fig. 2. Dynamic mechanical response of the as-built specimen and quenched specimens. (a) Engineering stress vs. engineering strain curves. (b) True stress vs. true strain curves. (c) Comparisons of the yield strength, ultimate compressive strength and impact energy. (d) Impact energy of different materials [36–47].

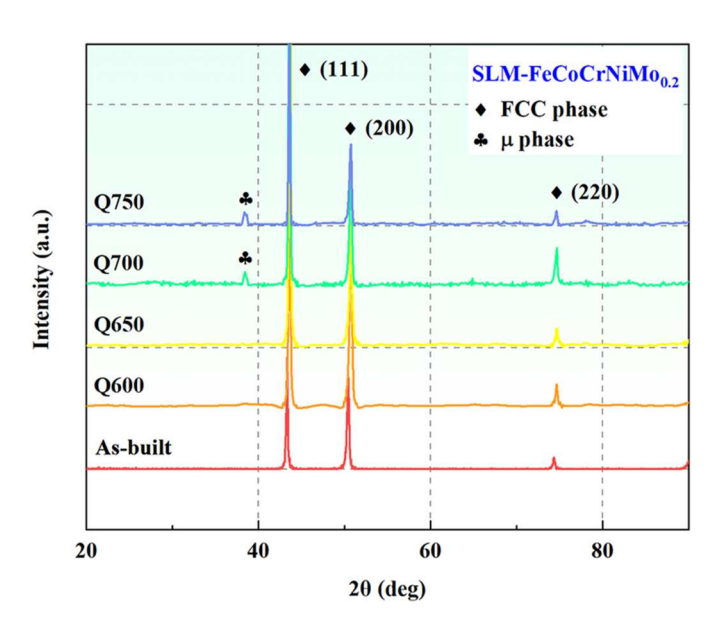


Fig. 3. XRD pattern of the as-built specimen and quenched specimens [35].

 μ phase, respectively. The morphology, crystal structure, and element distribution of the μ phase are consistent with those reported in the literature [1].

Fig. 9 depicts the small-angle neutron-scattering results for various specimens, including the as-built specimen and the quenched specimens. As presented in Fig. 9(a), the scattering intensity of the quenched specimens are slightly higher compared to that of the as-built specimen, gradually increasing with higher heating temperatures. In order to deduce the evolution of the volume fraction and size of μ phase, an invariant is calculated using Sasview software based on the small-angle neutron-scattering dates [49]. For FeCoNiCrMo_{0.2} HEAs systems with FCC matrix and μ phase, Q* are given as follows [50,51]:

$$Q^* = \int_0^\infty q^2 I(q) dq \tag{1}$$

$$Q^* = 2\pi^2 (\Delta \rho)^2 \varphi_1 \varphi_2 \tag{2}$$

In equation (1), Q^* could be calculated as the area of the small angle neutron-scattering curves. In equation (2), $\Delta \rho$ is the difference between the scattering-length density of the second phases and matrix, φ_1 and φ_2 are the volume fractions of the second phases and matrix, respectively $(\varphi_1 + \varphi_2 = 1)$. The effective radius is obtained after fitting, and the average sizes (twice the effective radius) of μ phase are obtained from the fitting parameters. Detailed calculations of the volume fractions and sizes can be found in Appendix B. Fig. 9(b) displays the volume fractions and average sizes of μ phases in different specimens. It is indicated that

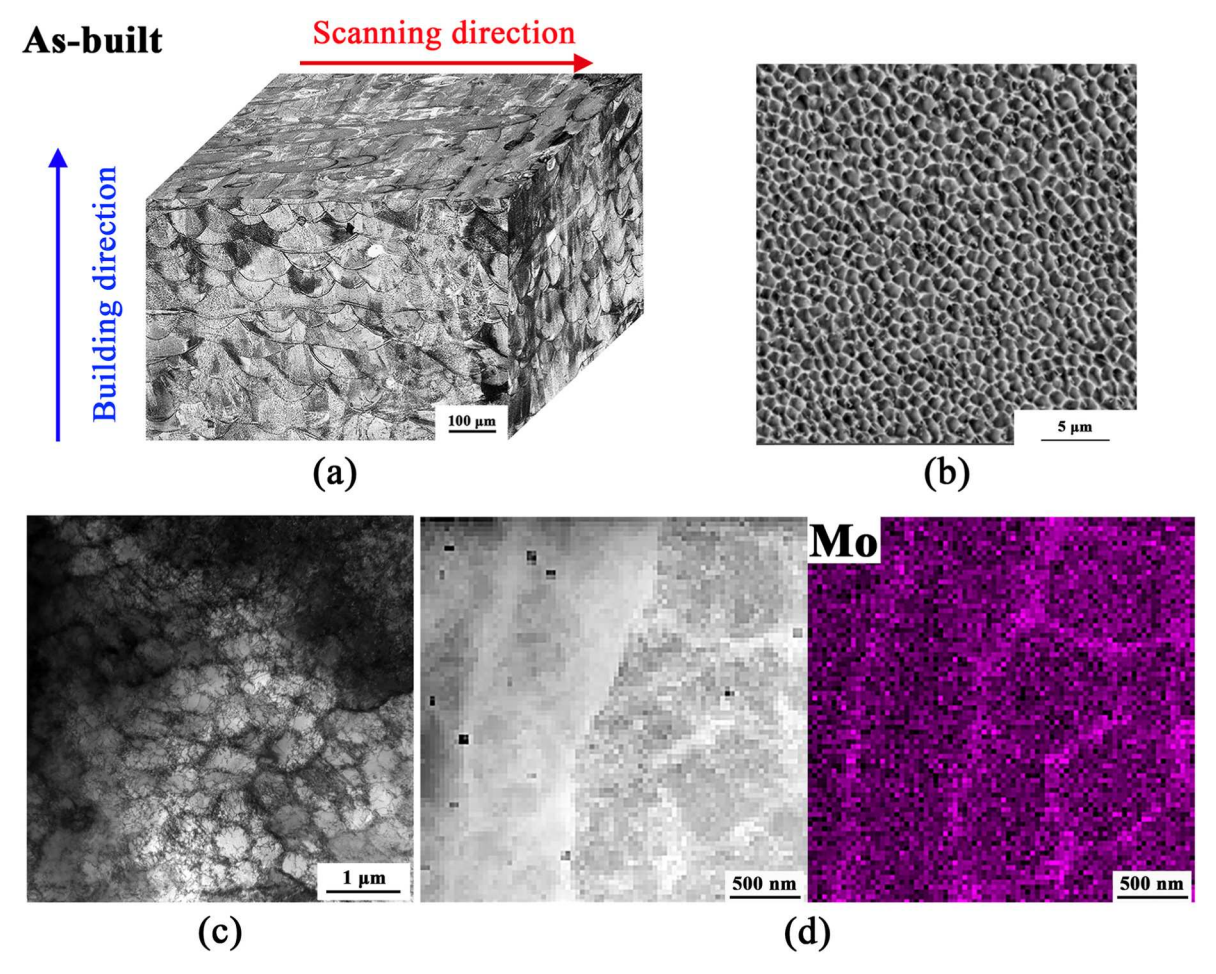


Fig. 4. Microstructure of the as-built specimen. (a) Optical image of the melt pool. (b) Fine cellular structures inside the melt pool. (c) Bright-field image of the cellular structures. (d) Mo segregation at boundary of cellular structure [35].

the volume fraction and average size of μ phases in the as-built specimen are 0.09 % and 60.4 nm, respectively. These value are very low so that the μ phases in the as-built specimen are difficult to observe. Subsequently, with the increasing heating temperature from 600 °C to 750 °C, the volume fraction and average sizes of the μ phases gradually increase. After heating at 750 °C, the volume fraction and average size of the μ phases in the Q750 specimen reach 4.0 % and 65.4 nm, respectively. It is worth mentioning that the average size of the μ phases shows limited variation with heating temperature, while the volume fraction exhibits a more significant change. This may be attributed to the fact that within the selected wavelength range, SANS technology can only identify μ phases with sizes below 100 nm. Particles larger than 100 nm are not included in the data analysis.

3.3. Deformed microstructure of SLM-FeCoNiCrMo_{0.2} HEAs

To further investigate the deformation mechanism of the cellular structure and μ phases under high strain-rate deformation, the microstructure of the as-built specimen, Q700 specimen and Q750 specimen after dynamic deformation was characterized. In as-built specimen, there are no obvious micro-pores or micro-cracks, and the cellular structures undergo significant elongation along the dynamic deformation direction with their length exceeding 1 μm , as shown in Fig. 10(a). In Q700 specimen, the size of elongated cellular structures is noticeably smaller compared to the as-built specimen, and micro-cracks along the grain boundary are observed, as depicted in Fig. 10(b). Further generation of micro-pores along the cellular structures in Q750 specimen is presented in Fig. 10(c). Fig. 10(d) exhibits the TEM of Q700 specimen

after impact deformation. There are no apparent changes in the size and shape of μ phases. However, high-density dislocation appears near the μ phases marked in the blue box. It is suggested that the μ phases can impede the dislocation movement during impact deformation. Moreover, the boundary of the elongated cellular structures merge into the high-density dislocation regions. This trend may be attributed to the precipitation of the μ phases, which serve as obstacles at the boundary of the cellular structures, thus hindering their deformation during the impact deformation.

4. Discussion

4.1. Effect of the Mo segregation on the μ phases in the SLM-FeCoNiCrMo_{0.2} HEAs

It is reported that various factors such as initial grain size and element distribution in the as-built AM alloys can significantly affect the distribution, size, shape, and fraction of precipitates upon heat treatment [26–28]. In the SLM-FeCoNiCrMo $_{0.2}$ HEAs, the precipitation of second phases is influenced by Mo segregation and heating temperature. The rapid heating and cooling rates of the SLM process lead to segregation Mo at the boundary of cellular structures in the as-built specimen. Subsequent heating and quenching treatments facilitate the precipitation of Mo-rich second phases at the boundary. To investigate the effect of heating temperature and Mo content on precipitation of second phase in SLM-FeCoNiCrMo $_{0.2}$ HEA, a (FeCoNiCr)–Mo binary phase diagram was constructed using Pandat thermodynamic software [52], as shown in Fig. 11. The distribution of Mo in the alloy was categorized into two

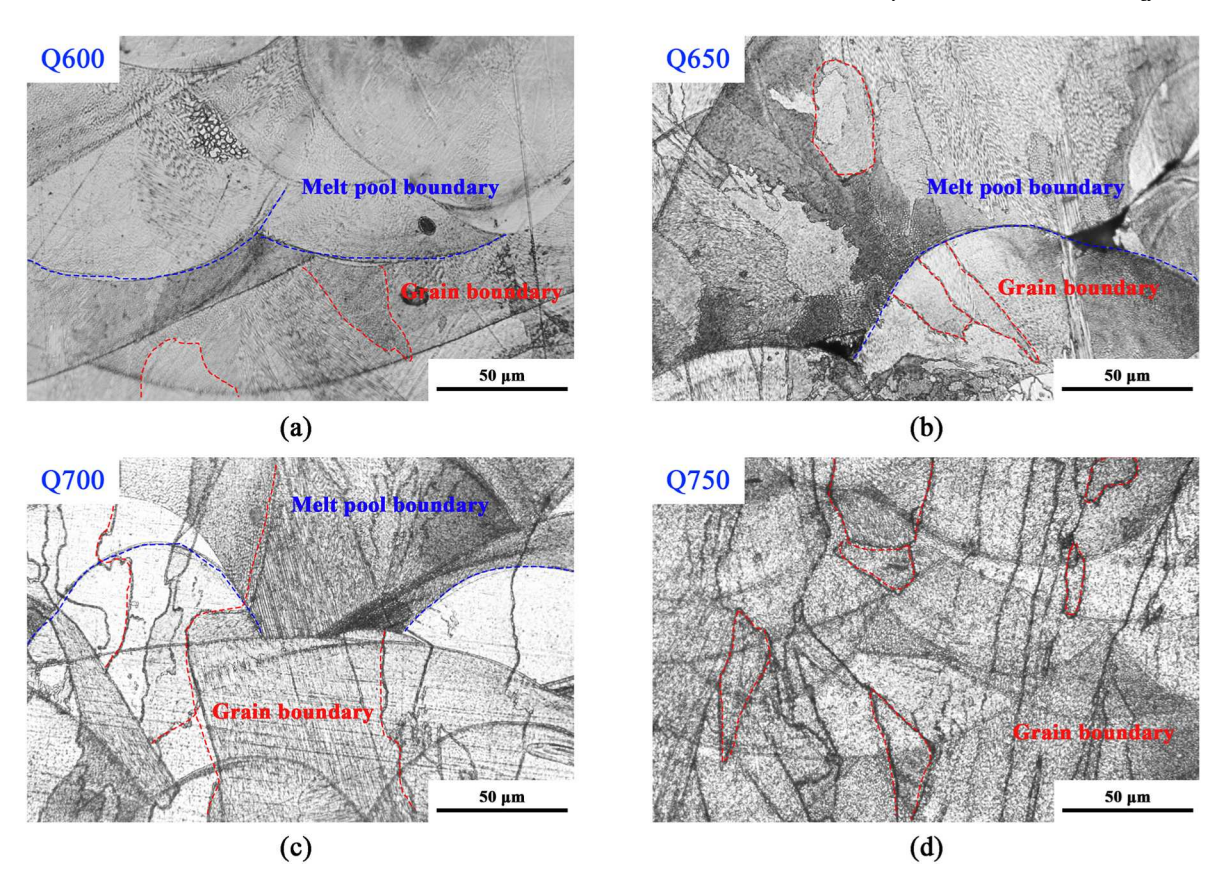


Fig. 5. Microstructure of the melt pool and columnar grain in the quenched specimens. (a) Q600 specimen. (b) Q650 specimen. (c) Q700 specimen. (d) Q750 specimen.

regions, Mo-rich micro-regions (with a Mo atomic fraction of 10%) at the boundary of cellular structure and Mo-poor micro-regions (with a Mo atomic fraction of 4%) within the cellular structure. The phase composition in the Mo-rich regions of the alloy consisted of FCC+ σ + μ phases at 600 °C, 650 °C, and 700 °C. When the heating temperature above 750 °C, the phase composition transfers to FCC+ σ phases. The phase composition in the Mo-poor regions of the alloy at the aforementioned temperatures remained FCC+ σ phases. Hence, lower temperatures and higher Mo enrichment contribute to the formation of the μ phase and the theoretical phase composition in the Q700 specimen is considered to be FCC+ σ + μ phases. In this work, relatively low heating temperatures were chosen to suppress excessive growth of the cellular structure while exploiting the Mo segregation present in the as-built specimens to achieve second phase precipitation at specific locations. Considering the similar strengthening effects of σ and μ phases as hard phases compared to the FCC phase [48,53,54], and in accordance with the experimental results obtained from XRD and TEM analyses, the second phase in the Q700 specimen is regarded as a single μ phase.

4.2. Deformation mechanism of the μ precipitates-strengthened SLM-FeCoNiCrMo_{0.2} HEAs

In the as-built specimen, the cellular structures play a crucial role in the dynamic deformation. The elongated cellular structures could disperse large impact strain and coordinate high strain-rate impact deformation. The impact deformation leads to a significant increase in dislocation density within the alloy, resulting in dislocation entanglement. The elongated cellular structures are severed and fragmented into multiple smaller dislocation cell structures by the dislocation wall, further synergizing the impact deformation [35]. While in the quenched Q700 specimen, the distributed μ phases at the boundary can pin down the boundary, resulting in inhibiting the elongation of cellular

structures. Generally, stress waves are transmitted during impact deformation, and larger second phases can induce locally higher reverse tensile stresses, leading to brittle fracture of the material [55-57]. However, dispersed nanoscale second phases can activate multiple deformation mechanisms, impeding crack propagation in the material [58,59]. In the Q700 specimen, the size of the μ phases is approximately 63.4 nm, allowing it to simultaneously anchor boundary of the cellular structure and undergo coordinated deformation, thus mitigating impact damage. Fig. 12 exhibits the schematic diagram of the microstructure evolution in the SLM-FeCoNiCrMo_{0,2} HEAs. There are fine cellular structures with the Mo segregation at the boundary in the as-built specimen. During the heating and quenching process, the μ phases precipitated at the boundary of the coarsening cellular structures in the quenched specimen. After impact deformation, the cellular structures in the as-built specimens are elongated with high-density dislocation at boundary to absorb impact energy. In the quenched specimens, the $\boldsymbol{\mu}$ phases impede dislocation motion and anchor the boundary, resulting in finer elongated cellular structures compared to the as-built specimens. Additionally, the nanoscale μ phases can also undergo coordinated deformation along with cellular structures, further enhancing the impact toughness of the SLM-FeCoNiCrMo_{0.2} HEAs.

4.3. Strengthening mechanism of the SLM-FeCoNiCrMo_{0.2} HEAs

At a strain rate of $1840~s^{-1}$, the yield strength of the quenched Q700 specimen is 1066~MPa, which is 52.7% higher than that of the as-built specimen. Heating and quenching treatment result in the coarsening of grains and cellular structures, reduced dislocation density, and precipitation of second phases as the primary mechanisms of microstructural evolution in the SLM-FeCoNiCrMo_{0.2} HEAs. These collectively determine the enhancement of dynamic yield strength. Here, the contributions of different microstructures to the yield strength are

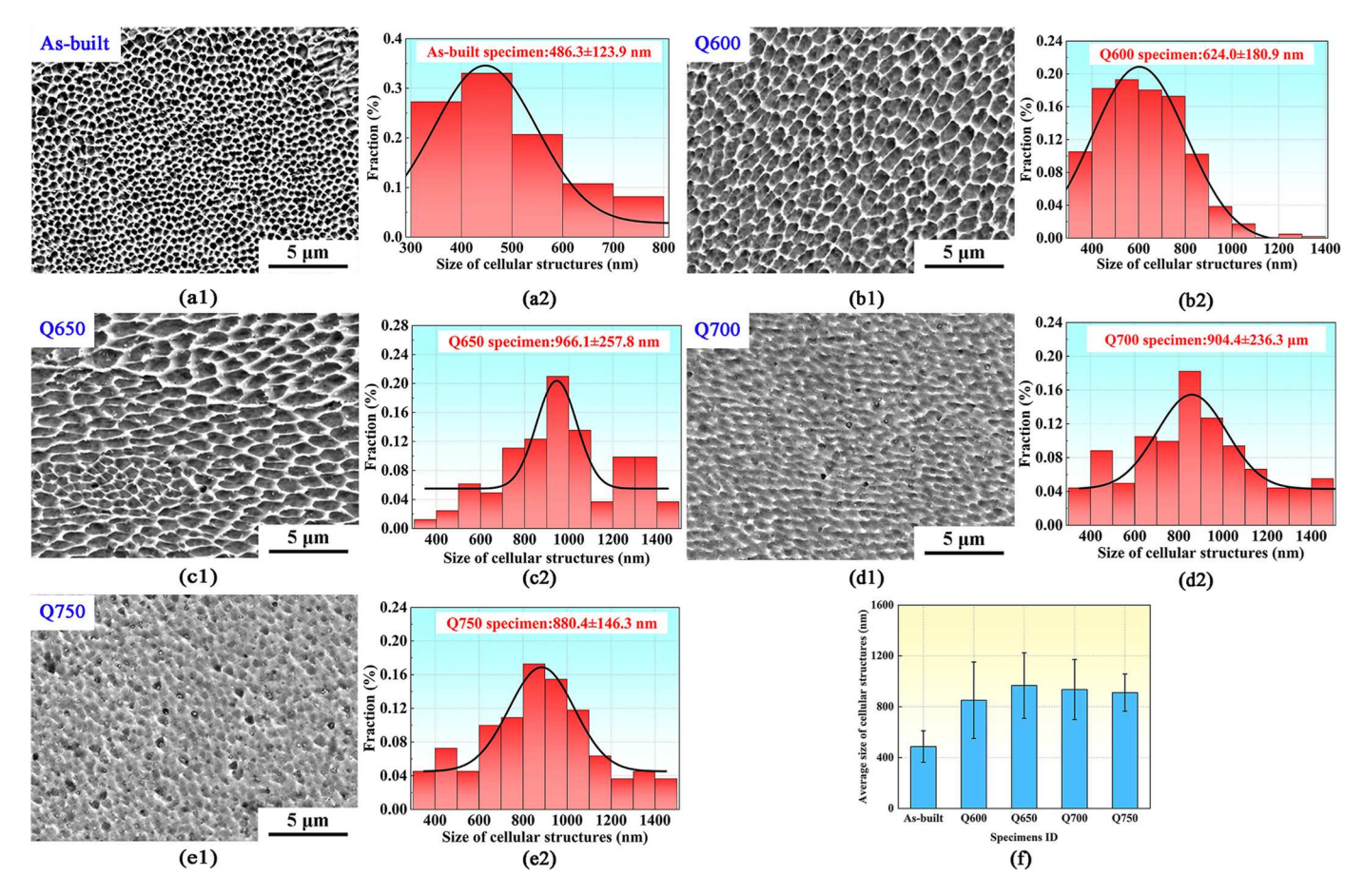


Fig. 6. Microstructure and size distributions of the cellular structures in the as-built specimen and quenched specimens. (a1-e1) Cellular structures in various specimens. (a2-e2) Corresponding size distributions in the different specimens. (f) The average size of the cellular structures in different specimens.

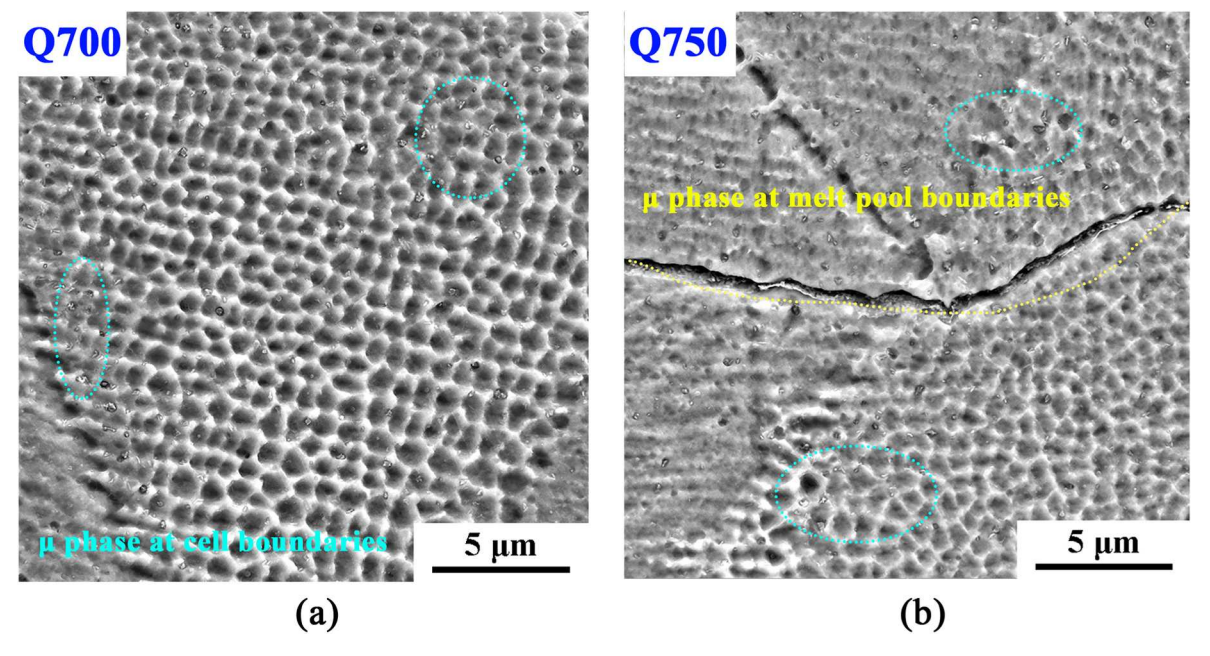


Fig. 7. The μ phases in the Q700 specimen and Q750 specimen. (a) Q700 specimen. (b) Q750 specimen.

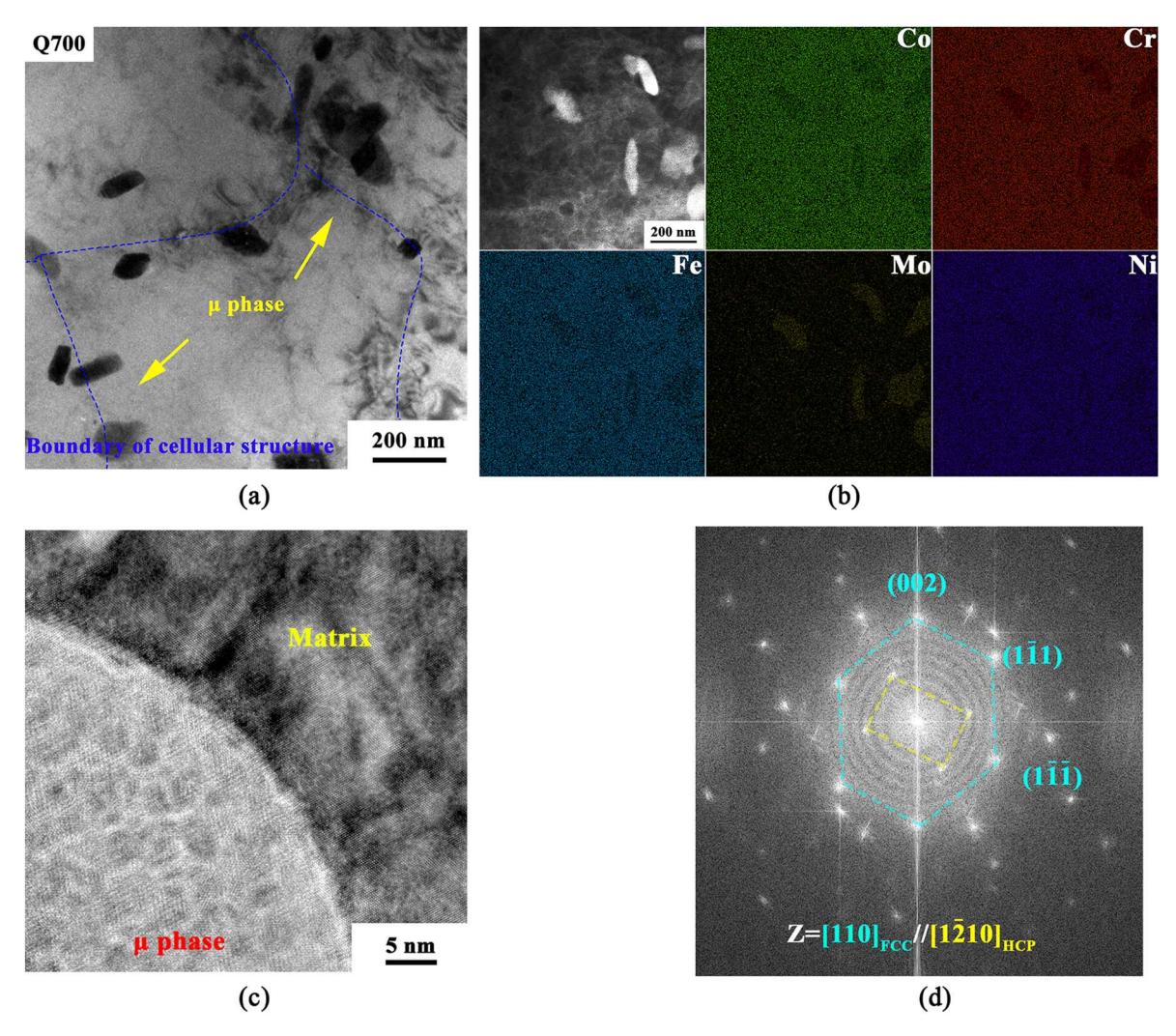


Fig. 8. TEM image of μ phases in the Q700 specimen. (a) Bright-field image. (b) Elemental distribution of the μ phases. (c) High-resolution TEM image of μ phases. (d) Diffraction pattern of μ phases and matrix.

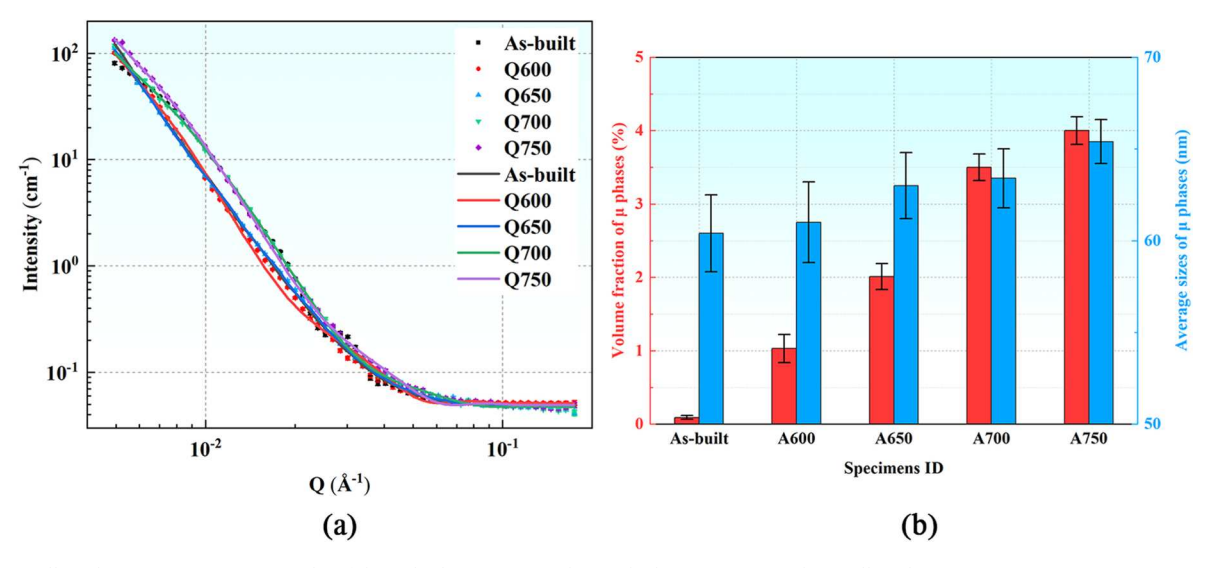


Fig. 9. The small-angle neutron-scattering results of the as-built specimen and quenched specimens. (a) The small angle neutron-scattering curves measured at room temperature of different specimens. (b) The volume fraction and average size of μ phases calculated from the small angle neutron scattering curves.

quantitatively calculate to explore the main strengthening mechanisms.

The strengthening contributions include the lattice-frictional strength, σ_f , solid-solution strengthening, σ_{SS} [60], grain-boundary strengthening σ_{GB} [61], dislocation strengthening σ_ρ [62], and precipitation strengthening σ_{pre} . The yield strength, σ_y , can be calculated by the following equation:

$$\sigma_{y} = \sigma_{f} + \sigma_{SS} + \sigma_{GB} + \sigma_{\rho} + \sigma_{pre} \tag{3}$$

Generally speaking, equation (3) refers to the yield strength of materials under quasi-static conditions. To account for the influence of strain rate on the yield strength, the Johnson-Cook constitutive equation is employed to describe the relationship between strain rate and flow stress. The expression is given as follows [63]:

$$\sigma = (A + B\varepsilon^n) \left[1 + C \left(\ln \frac{\dot{\varepsilon}}{\dot{\varepsilon}_0} \right)^m \right] \left[1 - D \left(\frac{T - T_0}{T_0} \right)^k \right]$$
 (4)

where σ represents the flow stress, ε is the strain, $\dot{\varepsilon}$ is the strain rate, T is the deformation temperature. $\dot{\varepsilon}_0=0.01~{\rm s}^{-1}$ and $T_0=298~{\rm K}$ are the reference strain rate and reference temperature, respectively. A,B,C,D,n,m,k are materials parameters. In equation (4), the first term reflects the strain hardening of the material. In the absence of strain rate and deformation temperature considerations, the value of the yield strength is approximately equal to the flow stress at a strain of 0.2%. The second term reflects the strain rate hardening of the material. The third term reflects the thermal softening effect of the material, considering the adiabatic temperature rise during dynamic deformation process. In this work, the dynamic yield strength of SLM-FeCoNiCrMo_{0.2} HEAs can be expressed as follows:

$$\sigma_{dys} = (A + B0.002^n) \left[1 + C \left(ln \frac{\dot{\varepsilon}}{0.01} \right)^m \right] \left[1 - D \left(\frac{T - T_0}{T_0} \right)^k \right]$$
 (5)

In this equation, the value of the first term is approximately equal to σ_y in equation (3). Substituting equation (3) into equation (5), we obtain

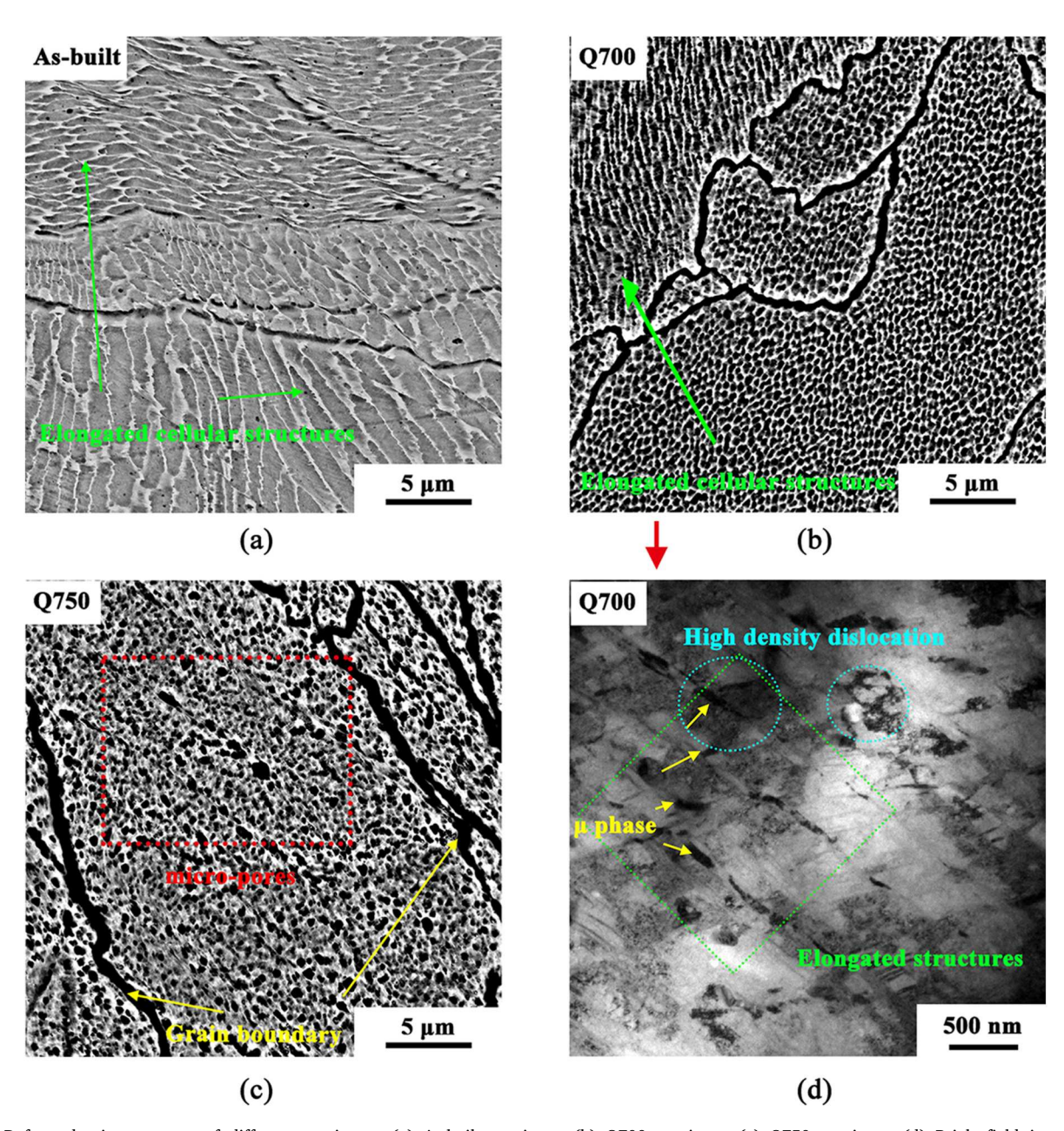


Fig. 10. Deformed microstructure of different specimens. (a) As-built specimen. (b) Q700 specimen. (c) Q750 specimen. (d) Bright-field images of the Q700 specimen.

the following expression:

$$\sigma_{dys} = \left(\sigma_f + \sigma_{SS} + \sigma_{GB} + \sigma_{\rho} + \sigma_{pre}\right) \left[1 + C\left(ln\frac{\dot{\varepsilon}}{0.01}\right)^m\right] \left[1 - D\left(\frac{T - T_0}{T_0}\right)^k\right]$$

The following conditions are assumed: First, the strain-rate strengthening factors affect differently to the various strengthening mechanisms, indicating that different microstructures have different sensitivities to strain rate. Second, the lattice stress and initial solid-solution strengthening, as the initial strength of the alloys, are independent of strain rate. Third, the value of m is the same among the different strain-rate strengthening factors. equation (6) could be further recast into the following expression:

$$\rho = 2\sqrt{3}\varepsilon / Db \tag{10}$$

$$\beta \cos \theta = K\lambda/D + 4\varepsilon \sin \theta \tag{11}$$

where the constant M, known as the Taylor factor, is set at 3.06 [65]. The values α (0.33), G (76 GPa), and b (0.255 nm) correspond to the shear modulus and burger vector for FCC phase [65,66]. In equation (10), ρ represents the dislocation density, ε refers to the micro-strain. In equation (11), θ , β , and λ represent the Bragg angle, the corresponding peak broadening, and the wavelength in the XRD pattern, respectively. The dislocation density of the as-built specimens is calculated to be about $1.28 \times 10^{14}~\rm nm^{-2}$. As the annealing temperature increases, the dislocation density exhibits a decreasing trend. In contrast, the size of the

$$\sigma_{dys} = \left\{ \left(\sigma_f + \sigma_{SS} \right) + \sigma_{GB} \left[1 + a_1 \left(ln \frac{\dot{\varepsilon}}{0.01} \right)^m \right] + \sigma_{\rho} \left[1 + a_2 \left(ln \frac{\dot{\varepsilon}}{0.01} \right)^m \right] + \sigma_{pre} \left[1 + a_3 \left(ln \frac{\dot{\varepsilon}}{0.01} \right)^m \right] \right\} \left[1 - D \left(\frac{T - T_0}{T_0} \right)^k \right]$$

$$(7)$$

where a_1 , a_2 , a_3 , represent the strain-rate strengthening factors associated with the grain boundary strengthening, precipitation strengthening, and dislocation strengthening. To fit the parameters a_1 , a_2 , a_3 , m, p, k, the strength contributions of different strengthening mechanisms were calculated for the as-built specimen and quenched specimens.

The total value of the lattice-frictional strength, σ_f , and solid-solution strength, σ_{SS} , is evaluated to be 90.3 MPa, which is the same in different specimens [35]. The grain-boundary strengthening σ_{GB} is inversely proportional to grain size, which is given by Ref. [64]:

$$\sigma_{GB} = kd^{-1/2} \tag{8}$$

where k is the strengthening coefficient (~494 MPa \times µm^{0.5} [35]), and the d is the average grain size. The average grain size d of the as-built specimens is approximately 21.4 µm. As the heating temperature increases, the grain size in the quenched specimens gradually increases, reaching a peak value at approximately 31.8 µm in the Q750 specimen. Table 5 provides the average grain sizes along with their corresponding grain boundary strengthening contributions in different specimens, which decrease with the increasing heating temperature.

The contribution of the dislocation strengthening, σ_{ρ} , is related to dislocation density and size of the cellular structures [66], which is expressed as follows:

$$\sigma_{o} = M\alpha G b \sqrt{\rho} \tag{9}$$

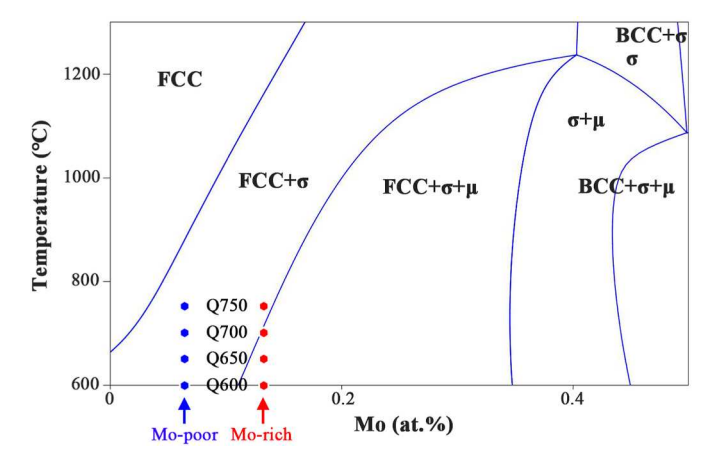


Fig. 11. Binary phase diagram of (FeCoNiCr)-Mo HEAs.

cellular structures exhibits an opposing trend, increasing as the annealing temperature rises. This increase in size of the cellular structures, coupled with a decrease in dislocation density, ultimately leads to a gradual weakening of dislocation strengthening. The dislocation density, sizes of the cellular structures and corresponding dislocation strengthening value of different specimens are given in Table 6.

The precipitation strengthening, $\sigma_{\rho re}$, can be accounted using the modulus hardening due to the result that the size of the μ phase is less than 100 nm [2,3], which can be described as follows [2]:

$$\Delta \sigma_{modulus} = \frac{M\Delta G}{4\pi^2} \left(\frac{3\Delta G}{Gb}\right)^{1/2} \left[\left(0.8 - 0.143 \ln\left(\frac{r}{b}\right)\right) \right]^{2/3} r^{1/2} f^{1/2}$$
 (12)

where r refers to the average size of the μ phases, and f refers to the volume fraction of μ phases, and ΔG refers to the difference between the shear modulus of the FCC matrix and shear modulus of the μ phases. The shear modulus of the μ phases can be calculated from its elastic modulus, which has been reported to be 249 GPa [67]. Therefore, the shear modulus of the μ phases is approximately 124.5 GPa, resulting in a value of the ΔG equal to 48.5 GPa. Combined with the results from Fig. 7, the precipitation strengthening value of the as-built specimens is approximately 105.9 MPa. After annealing and quenching, the volume fraction of the μ phases could increase, resulting in increased precipitation strengthening. The average size of μ phases, volume fraction of the μ phases, and corresponding precipitation strengthening value of different specimens are presented in Table 7.

At strain rate of 1800 s⁻¹, the deformation process is considered adiabatic. The deformation energy transforms into an increase in temperature. We evaluate the adiabatic temperature rise using the following formula [36]:

$$T = T_0 + \Delta T = T_0 + \frac{\eta}{\rho C_v} \int_{\varepsilon_v}^{\varepsilon_e} \sigma d\varepsilon$$

where T_0 and ΔT are the initial temperature and temperature rise during deformation, respectively. η , ρ , C_{ν} , refer to the fraction of the plastic energy, mass density of HEAs, and the heat capacity. $\int_{\epsilon_s}^{\epsilon_e} \sigma d\epsilon$ can be calculated from stress vs. strain curves from Fig. 2. In this work, η is 0.9, ρ is 8.117 g/cm³, C_{ν} is 0.43 J/(g·K), T_0 is 298 K [68]. Simultaneously, the dynamic mechanical responses of the as-built specimen under different strain rates are also taken into consideration. In addition to the strain rate of 1840 s⁻¹, dynamic mechanical performance and adiabatic temperature rise of the as-built specimens at strain rates of 1520 s⁻¹, 2070 s⁻¹, and 2310 s⁻¹ are evaluated. The stress vs. strain curves of the

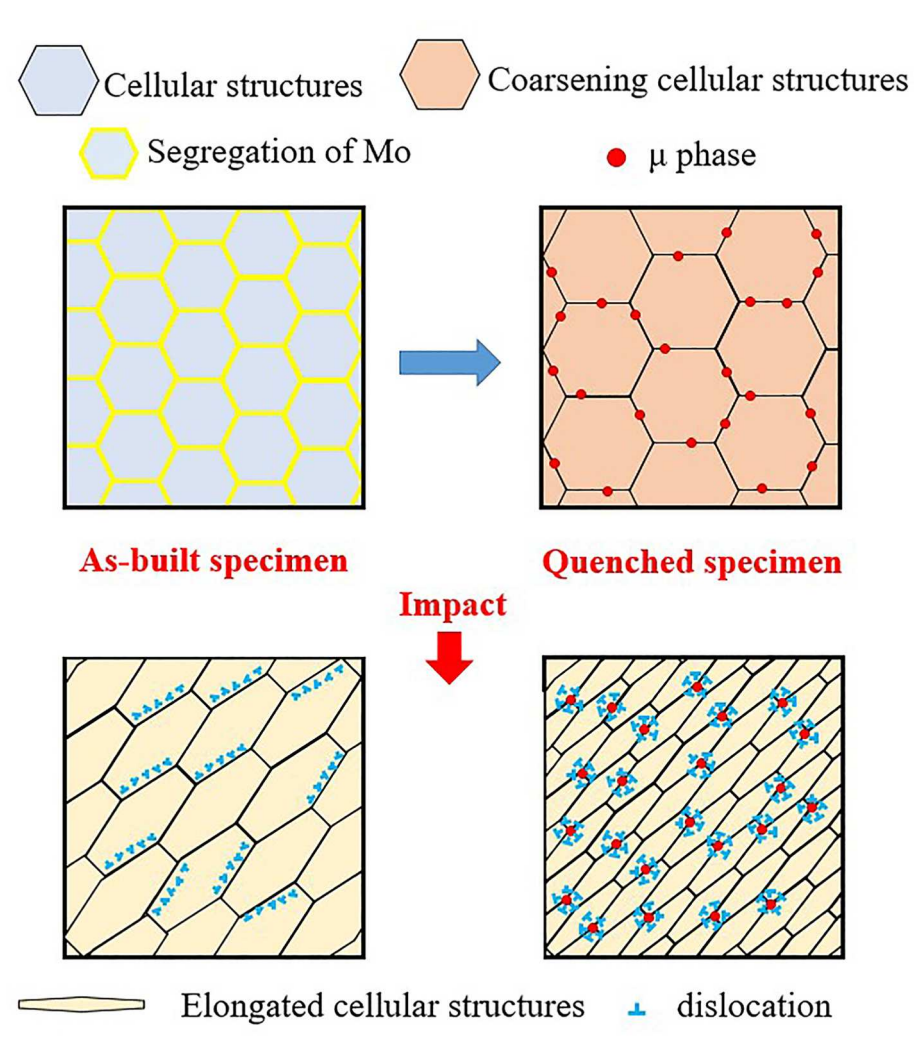


Fig. 12. Schematic diagram of the microstructure evolution of the cellular structures and μ phases in the SLM-FeCoNiCrMo_{0.2} HEAs.

as-built specimens at strain rates of $1520 \, s^{-1}$, $2070 \, s^{-1}$, and $2310 \, s^{-1}$ are given in Appendix C. The adiabatic temperature rises of the as-built specimen and quenched specimens are shown in Table 8.

According to the strengthening mechanism analysis above, the parameters a_1 , a_2 , a_3 , m, D, k in equation (7) can be fitted using MATLAB software by substituting the calculation results into equation (7). The fitting results of the parameters are shown in Table 9 and the modified equation is as follows:

In the as-built SLM-FeCoNiCrMo $_{0.2}$ HEAs, there is Mo segregation at the boundary of fine cellular structures. The fine cellular structure with high-density dislocation at the boundary plays a major strengthening role. After annealing and quenching, the coarsening cellular structures and precipitation of the μ phases occur in the quenched SLM-FeCo-NiCrMo $_{0.2}$ HEAs. When annealing temperatures range from 600 to 750 °C, higher heating temperatures result in larger sizes of the cellular structures, lower dislocation density, and increased sizes and volume

$$\sigma_{dys} = \left\{ \left(\sigma_f + \sigma_{SS} \right) + \sigma_{GB} \left[1 + 1.69 \times 10^{-5} \left(ln \frac{\dot{\varepsilon}}{0.01} \right)^{5.05} \right] + \sigma_{\rho} \left[1 + 8.74 \times 10^{-6} \left(ln \frac{\dot{\varepsilon}}{0.01} \right)^{5.05} \right] + \sigma_{pre} \left[1 + 1.55 \times 10^{-7} \left(ln \frac{\dot{\varepsilon}}{0.01} \right)^{5.05} \right] \right\} \left[1 - 0.902 \left(\frac{\Delta T}{298} \right)^{0.288} \right]$$

$$(13)$$

equation (13) expresses the relationship between the dynamic yield strength and microstructure of SLM-FeCoNiCrMo $_{0.2}$ HEAs under the condition of the strain rates range from 1500 to 2340 s $^{-1}$. Table 10 presents the comparison between the results calculated from equation (13) and the experimental values, along with the calculation of the error of this model. The average error of this model is approximately 8.97%, indicating that this model could effectively predict the dynamic yield strength of SLM-FeCoNiCrMo $_{0.2}$ HEAs at a strain rates range from 1500 to 2340 s $^{-1}$.

fractions of the μ phases. The coarsening microstructure leads to a reduction in grain boundary strengthening, the decrease in dislocation density results in a decline in dislocation strengthening, and the increase in volume fraction of the μ phases contributes to an enhancement in precipitation strengthening. The synergistic strengthening mechanisms led to the improvement of dynamic mechanical properties of the quenched SLM-FeCoNiCrMo_0.2 HEAs and precipitation strengthening plays a major strengthening role. It is worth mentioned that in the quenched specimens, dislocation strengthening and grain-boundary

Table 5Average grain sizes and corresponding grain boundary strengthening in different specimens.

Specimens ID	As-built	Q600	Q650	Q700	Q750
Grain size (µm)	21.4	23.6	27.3	29.5	31.8
σ_{GB} (MPa)	106.8	101.6	94.6	91.0	87.6

Table 6Dislocation density, size of the cellular structures and corresponding dislocation strengthening in different specimens.

Specimens ID	As-built	Q600	Q650	Q700	Q750
Dislocation density (nm ⁻²) Size of cellular	$1.28 \times 10^{14} \times 483.6$	6.71 × 10 ¹³ 850.0	5.82 × 10 ¹³ 966.0	5.55 × 10 ¹³ 904.4	5.41 × 10 ¹³ 880.4
structures (nm) σ_{ρ} (MPa)	221.7	160.3	149.3	145.9	143.9

Table 7 Average size of μ phases, volume fraction of μ phases and corresponding precipitation strengthening in different specimens.

Specimens ID	As-built	Q600	Q650	Q700	Q750
Average size of μ phases (nm)	60.4	61.0	63.1	63.4	65.4
Volume fraction of μ phases (%)	0.09	1.03	2.01	3.5	4
$\sigma_{\rho re}$ (MPa)	105.9	341.3	390.7	491.2	381.1

strengthening still contribute to a certain extent of strengthening effect. When the annealing temperature is too high, the contributions of both factors further decrease, and the growth of the μ phases also weakens the precipitation strengthening, resulting in the reduced mechanical properties of the SLM-FeCoNiCrMo_{0.2} HEAs.

5. Conclusion

In this study, a nanoscale precipitate-strengthened FeCoNiCrMo_{0.2} HEA was prepared by the selective laser melting and subsequent annealing and quenching. The dynamic-mechanical properties of an SLM-FeCoNiCrMo_{0.2} HEA reach peak values when the laser power, scanning speed, and annealing temperature are at 330 W, 800 mm/s, and 700 °C, respectively. The energy absorption, dynamic yield strength and ultimate compressive strength of the quenched Q700 SLM-FeCo-NiCrMo_{0.2} HEAs reached 214.5 MJ/m³, 1066 MPa and 1649 MPa, respectively, at the strain rate of 1840 s⁻¹. These values are 34.9%, 52.7%, and 17.2% higher compared with those of the as-built SLM-FeCoNiCrMo_{0.2} HEAs. There are fine cellular structures with the Mo segregation at the boundary of cellular structures in the as-built specimen, which provides the concentration condition for the precipitation. After subsequent annealing and quenching, the fine cellular structures are coarsened. Simultaneously, a number of nanoscale Mo-rich $\boldsymbol{\mu}$ phases are dispersedly contributed at boundary of cellular structures. These kinds of nanoscale μ phases are considered to be able to pin the boundary, hindering dislocation movement. They can also undergo coordinated deformation with cellular structures, further enhancing the

Table 9 Fitting results of the parameters a_1 , a_2 , a_3 , m, D, k.

Parameter	a_1	a_2	a_3	m	D	k
Value	1.69×10^{-5}	8.74×10^{-6}	1.55×10^{-7}	5.08	0.902	0.288

Table 10Calculated dynamic yield strength, experimental dynamic yield strength, and error of the model.

Specimens ID	Calculated σ_{dys} (MPa)	Experimental σ_{dys} (MPa)	Relative error (%)	Average error (%)
As-built	585	698	16.4	8.97
Q600	889	1032	9.2	
Q650	949	985	0.4	
Q700	1099	1066	6.3	
Q750	922	1006	2.9	
As-built at 1520 s^{-1}	786	651	20.7	
As-built at 2070 s^{-1}	821	739	11.1	
As-built at 2310 s^{-1}	827	791	4.6	

impact toughness of the SLM-FeCoNiCrMo $_{0.2}$ HEAs. Under the given process parameters, the prepared high-entropy alloy achieved precipitation of μ phases while controlling the excessive coarsening of grain and cellular structures. The precipitation strengthening serves as the primary strengthening mechanism, synergistically enhancing the dynamic mechanical properties along with the dislocation strengthening and grain boundary strengthening.

Credit author contribution statement

Wenshu Li: Methodology, Formal analysis, Investigation, Data curation, Writing-original draft preparation, Writing-review and editing, Visualization. Ruovu Liu: Methodology, Formal analysis, Investigation, Data curation. Shaohong Wei: Methodology, Investigation, Data curation, Writing-original draft preparation, Writing-review and editing, Visualization. Yiyu Huang: Methodology, Data curation, Writing-review and editing, Visualization. Qi Wu: Methodology, Investigation, Data curation. Ao Fu: Formal analysis, Investigation. Yubin Ke: Methodology, Investigation, Data curation, Visualization, Supervision. Peter K. Liaw: Conceptualization, Validation, Formal analysis, Supervision. Bin Liu: Conceptualization, Validation, Formal analysis, Resources, Writing-review and editing, Supervision, Project administration, Funding acquisition. Bingfeng Wang: Conceptualization, Validation, Formal analysis, Investigation, Data curation, Writingoriginal draft preparation, Writing-review and editing, Supervision, Project administration, Funding acquisition.

Date availability

The raw/processed data required to reproduce these findings cannot be shared at this time as the data also forms part of an ongoing study.

Table 8Calculation of adiabatic temperature rises of the as-built specimen and quenched specimens.

	•		•					
Specimens ID	$\dot{\varepsilon}$ (s ⁻¹)	T (K)	T ₀ (K)	ΔT (K)	η	C_{ν} J/(g·K)	ρ (g/cm ³)	$\int_{\varepsilon_s}^{\varepsilon_e} \sigma d\varepsilon (\mathrm{J/cm}^3)$
As-built	1840	338.9	298	40.9	0.9	0.43	8.117	159
Q600	1800	351.1	298	53.1	0.9	0.43	8.117	206
Q650	1860	352.9	298	54.9	0.9	0.43	8.117	213
Q700	1830	353.1	298	55.1	0.9	0.43	8.117	214
Q750	1830	348.5	298	50.5	0.9	0.43	8.117	196
As-built	1520	333.6	298	35.6	0.9	0.43	8.117	138
As-built	2070	341.6	298	43.6	0.9	0.43	8.117	169
As-built	2310	344.9	298	46.9	0.9	0.43	8.117	182

Declaration of competing interest

The authors declare that they have no known competing financial interests or personal relationships that could have appeared to influence the work reported in this paper.

Acknowledgments

The present work was financially supported by the National Natural Science of China [grant number 52020105013], and by the State Key Laboratory of Powder Metallurgy [grant number 62102172]. Yubin Ke is grateful to the support from the National Natural Science Foundation of China [grant number 12275154] and the Youth Innovation Promotion Association, CAS [grant number 2020010]. P.K. Liaw very much appreciates the support from (1) the National Science Foundation [grant number DMR - 1611180, 1809640, and 2226508] and (2) the US Army Research Office [grant number W911NF-13-1-0438 and W911NF-19-2-0049]. The authors wish to express their most sincere gratitude to Professor Marc A. Meyers at the University of California, San Diego, and Professor Yong Liu at the Central South University, and Professor Yong Yang at the City University of Hong Kong for their advice and helps. The authors would like to thank the China Spallation Neutron Source for providing neutron beam time and help with SANS measurement and data-reduction. The authors would like to present their sincere thanks to Professors Xiang Zan at the University of Science and Technology of China, for the experimental works.

Appendix A. Supplementary data

Supplementary data to this article can be found online at $\frac{\text{https:}}{\text{doi.}}$ org/10.1016/j.jmrt.2024.03.113.

References

- Liu WH, Lu ZP, He JY, Luan JH, Wang ZJ, Liu B, et al. Ductile CoCrFeNiMox high entropy alloys strengthened by hard intermetallic phases. Acta Mater 2016;166: 332–42. https://doi.org/10.1016/j.actamat.2016.06.063.
- [2] Jiang SH, Wang H, Wu Y, Liu XJ, Chen HH, Yao MJ, et al. Ultrastrong steel via minimal lattice misfit and high-density nanoprecipitation. Nature 2017;544:460–4. https://doi.org/10.1038/nature22032.
- [3] Liang YJ, Wang LJ, Wen YR, Cheng BY, Wu QL, Cao TQ, et al. High-content ductile coherent nanoprecipitates achieve ultrastrong high-entropy alloys. Nat Commun 2018;9:4063. https://doi.org/10.1038/s41467-018-06600-8.
- [4] Oliveira JP, Santos TG, Miranda RM. Revisiting fundamental welding concepts to improve additive manufacturing: from theory to practice. Prog Mater Sci 2020;107: 100590. https://doi.org/10.1016/j.pmatsci.2019.100590.
- [5] Gu DD, Shi XY, Roprawe R, Bourell DL, Setchi R, Zhu JH. Material-structureperformance integrated laser-metal additive manufacturing. Science 2021;372 (6545):1487. https://doi.org/10.1126/science.abg1487.
- [6] Bermingham MJ, Stjohn DH, Krynen J, Tedman-Jones S, Dargusch MS. Promoting the columnar to equiaxed transition and grain refinement of titanium alloys during additive manufacturing. Acta Mater 2019;168:261–74. https://doi.org/10.1016/j. actamat.2019.02.020.
- [7] Kotadia HR, Gibbons G, Das A, Howes PD. A review of laser powder bed fusion additive manufacturing of aluminium alloys: microstructures and properties. Addit Manuf 2021;46:102155. https://doi.org/10.1016/j.addma.2021.102155.
- [8] Liu LF, Ding QQ, Zhong Y, Zou J, Wu J, Chiu Y-L, et al. Dislocation network in additive manufactured steel breaks strength-ductility trade-off. Mater Today 2018; 21(4):354–61. https://doi.org/10.1016/j.mattod.2017.11.004.
- [9] Gray III GT, Livescu V, Rigg PA, Trujillo CP, Cady CM, Chen SR, et al. Structure/ property (constitutive and spallation response) of additively manufactured 316L stainless steel. Acta Mater 2017;138:140–9. https://doi.org/10.1016/j. actamat.2017.07.045.
- [10] Zhan YN, Ma ZQ, Yu LM, Liu YC. New alloy design approach to inhibiting hot cracking in laser additive manufactured nickel-based superalloys. Acta Mater 2023; 247:118736. https://doi.org/10.1016/j.actamat.2023.118736.
- [11] Zhang YM, Yu YF, Wang L, Lin F, Yan WT. Dispersion of reinforcing micro-particles in the powder bed fusion additive manufacturing of metal matrix composites. Acta Mater 2022;235:118086. https://doi.org/10.1016/j.actamat.2022.118086.
- [12] Callanan JG, Black AN, Lawrence SK, Jones DR, Martinez DT, Martinez RM, et al. Dynamic properties of 316l stainless steel repaired using electron beam additive manufacturing. Acta Mater 2023;246:118636. https://doi.org/10.1016/j. actamat.2022.118636.
- [13] Debroy T, Wei LH, Zuback JS, Mukherjee T, Elmer JW, Milewski JO, et al. Additive manufacturing of metallic components - process, structure and properties. Prog Mater Sci 2018;92:112–224. https://doi.org/10.1016/j.pmatsci.2017.10.001.

- [14] Zhou YH, Zhang ZH, Wang YP, Liu G, Zhou SY, Li YL, et al. Selective laser melting of typical metallic materials: an effective process prediction model developed by energy absorption and consumption analysis. Addit Manuf 2018;25:204–17. https://doi.org/10.1016/j.addma.2018.10.046.
- [15] Kong DC, Dong CF, Wei SL, Ni XQ, Zhang L, Li RX, et al. S about metastable cellular structure in additively manufactured austenitic stainless steels. Addit Manuf 2021; 38:101804. https://doi.org/10.1016/j.addma.2020.101804.
- [16] Tong ZP, Ren XD, Jian JF, Zhou WF, Ren YP, Ye YX, et al. Laser additive manufacturing of FeCrCoMnNi high-entropy alloy: effect of heat treatment on microstructure, residual stress and mechanical property. J Alloys Compd 2019;785: 1144–59. https://doi.org/10.1016/j.jallcom.2019.01.213.
- [17] Kuzminova YO, Kudryavtsev EK, Han J-K, Kawasaki M, Evlashin SA. Phase and structural changes during heat treatment of additive manufactured CrFeCoNi highentropy alloy. J Alloys Compd 2021;889:161495. https://doi.org/10.1016/j. iallcom.2021.161495.
- [18] Peng HP, Xie SY, Niu PD, Zhang ZJ, Yuan TC, Ren ZQ, et al. Additive manufacturing of Al_{0.3}CoCrFeNi high-entropy alloy by powder feeding laser melting deposition. J Alloys Compd 2020;862:158286. https://doi.org/10.1016/j. jallcom.2020.158286.
- [19] Vikram RJ, Murty BS, Fabijanic D, Suwas S. Insights into micro-mechanical response and texture of the additively manufactured eutectic high entropy alloy AlCoCrFeNi_{2.1}. J Alloys Compd 2020;827:154034. https://doi.org/10.1016/j. jallcom.2020.154034.
- [20] Gao XY, Yu ZJ, Hu WH, Liu Y, Zhu ZY, Ji Y, et al. In situ strengthening of CrMnFeCoNi high-entropy alloy with Al realized by laser additive manufacturing. J Alloys Compd 2020;847:156563. https://doi.org/10.1016/j. iallcom.2020.156563.
- [21] Park JM, Asghari-Rad P, Zargaran A, Bae JW, Moon J, Kwon H, et al. Nano-scale heterogeneity-driven metastability engineering in ferrous medium-entropy alloy induced by additive manufacturing. Acta Mater 2021;221:117426. https://doi. org/10.1016/j.actamat.2021.117426.
- [22] Shen QK, Kong XD, Chen XZ. Significant transitions of microstructure and mechanical properties in additively manufactured Al–Co–Cr–Fe–Ni high-entropy alloy under heat treatment. Mater Sci Eng, A 2021;815:141257. https://doi.org/ 10.1016/j.msea.2021.141257.
- [23] Lin W-C, Chang Y-J, Hsu T-H, Gorsse S, Sun F, Furuhara T, et al. Microstructure and tensile property of a precipitation strengthened high entropy alloy processed by selective laser melting and post heat treatment. Addit Manuf 2020;36:101601. https://doi.org/10.1016/j.addma.2020.101601.
- [24] Fujieda T, Shiratori H, Kuwabara K, Hirota M, Kato T, Yamanaka K, et al. CoCrFeNiTi-based high-entropy alloy with superior tensile strength and corrosion resistance achieved by a combination of additive manufacturing using selective electron beam melting and solution treatment. Mater Lett 2017;189:148–51. https://doi.org/10.1016/j.matlet.2016.11.026.
- [25] Thapliyal S, Agrawal P, Agrawal P, Nene SS, Mishra RS, McWillimas BA, et al. Segregation engineering of grain boundaries of a metastable Fe-Mn-Co-Cr-Si high entropy alloy with laser-powder bed fusion additive manufacturing. Acta Mater 2021;219:117271. https://doi.org/10.1016/j.actamat.2021.117271.
- [26] Li RX, Kong DC, He KT, Dong CF. Superior thermal stability and strength of additively manufactured CoCrFeMnNi high-entropy alloy via NbC decorated submicro dislocation cells. Scripta Mater 2023;230:115401. https://doi.org/10.1016/ j.scriptamat.2023.115401.
- [27] Kong DC, Wang L, Zhu GL, Zhou YQ, Ni XQ, Song J, et al. Heat treatment effects on the metastable microstructure, mechanical property and corrosion behavior of Aladded CoCrFeMnNi alloys fabricated by laser powder bed fusion. J Mater Sci Technol 2022;138:171–82. https://doi.org/10.1016/j.jmst.2022.08.018.
- [28] Li J, Cheng X, Li Z, Zong X, Zhang SQ, Wang HM. Improving the mechanical properties of Al-5Si-1Cu-Mg aluminum alloy produced by laser additive manufacturing with post-process heat treatments. Mater Sci Eng, A 2018;735: 408-17. https://doi.org/10.1016/j.msea.2018.08.074.
- [29] Li GC, Li J, Tian XJ, Cheng X, He B, Wang HM. Microstructure and properties of a novel titanium alloy Ti-6Al-2V-1.5Mo-0.5Zr-0.3Si manufactured by laser additive manufacturing. Mater Sci Eng, A 2017;684:233–8. https://doi.org/10.1016/j. msea.2016.11.084.
- [30] Cheng JC, Qin HL, Zhao F, Pan RC, Wang QY, Bian YL, et al. Deformation and damage of equiatomic CoCrFeNi high-entropy alloy under plate impact loading. Mater Sci Eng, A 2023;862:144432. https://doi.org/10.1016/j.msea.2022.144432.
 [31] Fu A, Liu B, Li ZZ, Wang BF, Cao YK, Liu Y. Dynamic deformation behavior of a
- [31] Fu A, Liu B, Li ZZ, Wang BF, Cao YK, Liu Y. Dynamic deformation behavior of a FeCrNi medium entropy alloy. J Mater Sci Technol 2022;100:120–8. https://doi. org/10.1016/j.jmst.2021.05.049.
- [32] Meng J, Qiao Y, Chen Y, Liu T-W, Li T, Wang H-Y, et al. A high-entropy alloy syntactic foam with exceptional cryogenic and dynamic properties. Mater Sci Eng, A 2023;876:145146. https://doi.org/10.1016/j.msea.2023.145146.
- [33] Cao TQ, Zhang Q, Wang L, Wang L, Xiao Y, Yao JH, et al. Dynamic deformation behaviors and mechanisms of CoCrFeNi high-entropy alloys. Acta Mater 2023;260: 119343. https://doi.org/10.1016/j.actamat.2023.119343.
- [34] Huang YY, Li WS, Liu RY, Chen HY, Wu Q, Wei SH, et al. Dynamic mechanical properties and σ precipitates strengthening of a NiCrFeCoMo_{0.2} high-entropy alloy additively manufactured by selective laser melting. J Alloys Compd 2023;968: 172244. https://doi.org/10.1016/j.jallcom.2023.172244.
- [35] Li WS, Huang YY, Xie ZH, Chen HY, Li WH, Liu B, et al. Mechanical property and cellular structure of an additive manufactured FeCoNiCrMo_{0.2} high-entropy alloy at high-velocity deformation. J Mater Sci Technol 2023;139:156–66. https://doi. org/10.1016/j.imst.2022.08.013.
- [36] Li WS, Wang BF, Huang XX, Liu B, Brechtl J, Liaw PK. Mechanical behavior and shear band of a powder-metallurgy-fabricated CoCrFeMnNi high-entropy alloy

- during high strain-rate deformation. J Mater Res Technol 2022;21:1461–78. https://doi.org/10.1016/j.jmrt.2022.09.106.
- [37] Wang BF, Wang C, Liu B, Zhang XY. Dynamic mechanical properties and microstructure of an (Al_{0.5}CoCrFeNi)_{0.95}Mo_{0.025}Co_{0.025} high entropy alloy. Entropy 2019;21(12):1154. https://doi.org/10.3390/e21121154.
- [38] Liu RY, Yao XR, Wang BF. Mechanical properties and serration behavior of a NiCrFeCoMn high-entropy alloy at high strain rates. Materials 2022;13(17):3722. https://doi.org/10.3390/ma13173722.
- [39] Wang YZ, Jiao ZM, Bian GB, Yang HJ, He HW, Wang ZH, et al. Dynamic tension and constitutive model in Fe₄₀Mn₂₀Cr₂₀Ni₂₀ high-entropy alloys with a heterogeneous structure. Mater Sci Eng, A 2022;839:142837. https://doi.org/ 10.1016/j.msea.2022.142837.
- [40] Wang K, Jin X, Zhang Y, Liaw PK, Qiao JW. Dynamic tensile mechanisms and constitutive relationship in CrFeNi medium entropy alloys at room and cryogenic temperatures. Phys Rev Mater 2021;5:113608. https://doi.org/10.1103/ PhysRevMaterials.5.113608.
- [41] Chen HY, Li WS, Huang YY, Xie ZH, Zhu XB, Liu B, et al. Molten pool effect on mechanical properties in a selective laser melting 316 L stainless steel at highvelocity deformation. Mater Char 2022;194:112409. https://doi.org/10.1016/j. matchar.2022.112409.
- [42] Feng XC, Liu XY, Bai SX, Ye YC, Zong L, Tang Y. Mechanical properties and deformation behaviour of TWIP steel at different strain rates. Mater Sci Eng, A 2023;879:145182. https://doi.org/10.1016/j.msea.2023.145182.
- [43] Lloyd JT, Magagnosc DJ, Meredith CS, Limmer KR, Field DM. Improved dynamic strength of TRIP steel via pre-straining. Scripta Mater 2022;220:114941. https://doi.org/10.1016/j.scriptamat.2022.114941.
- [44] Li Z, Xia ZR, He SC, Wang FZ, Wu X, Zhang Y, et al. Dynamic mechanical properties of FGH4097 powder alloy and the applications of its constitutive model. J Mater Res Technol 2023;22:1165–84. https://doi.org/10.1016/j.jmrt.2022.11.173.
- [45] Amir B, Lomnitz A, Gale Y, Friedlander L, Samuha S, Sadot O. Effects of shell scanning and build orientation on dynamic properties of laser powder bed fusion AlSi10Mg alloy. Mater Sci Eng, A 2023;883:145521. https://doi.org/10.1016/j. msea 2023.145521
- [46] Zhang GH, Zhu ZW, Ning JG, Feng C. Dynamic impact constitutive relation of 6008-T6 aluminum alloy based on dislocation density and second-phase particle strengthening effects. J Alloys Compd 2023;932:167718. https://doi.org/10.1016/ i.iall.com.2022.167718.
- [47] Damavandi E, Nourouzi S, Rabiee SM, Jamaati R, Tiamiyu AA, Szpunar JA. Effects of prior ECAP process on the dynamic impact behaviors of hypereutectic Al-Si alloy. Mater Sci Eng, A 2020;793:139902. https://doi.org/10.1016/j. msea.2020.139902.
- [48] Niu ZZ, Wang YZ, Geng C, Xu J, Wang Y. Microstructural evolution, mechanical and corrosion behaviors of as-annealed CoCrFeNiMox (x = 0, 0.2, 0.5, 0.8, 1) high entropy alloys. J Alloys Compd 2020;820:153273. https://doi.org/10.1016/j. iallcom.2019.153273.
- [49] Glatter O, Kratky O. Chatper 2 and chapter 14 in small angle X-ray scattering. New York: Academic press; 1982.
- [50] Shi R, Ma N, Wang Y. Predicting equilibrium shape of precipitates as function of coherency state. Acta Mater 2012;60:4172–84. https://doi.org/10.1016/j. actamat.2012.04.019.
- [51] Melnichenko YB. Chapter 6 in small-angle scattering from confined and interfacial fluids. Springer; 2016.
- [52] Zhu XZ, Dong XX, Blake P, Ji SX. Improvement in as-cast strength of high pressure die-cast Al-Si-Cu-Mg alloys by synergistic effect of Q-Al₅Cu₂Mg₈Si₆ and θ-Al₂Cu phases. Mater Sci Eng, A 2021;802:140612. https://doi.org/10.1016/j. msea.2020.140612.

- [53] Wu XL, Wang B, Rehm C, He HY, Naeem M, Lan S, et al. Ultra-small-angle neutron scattering study on temperature-dependent precipitate evolution in CoCrFeNiMo_{0.3} high entropy alloy. Acta Mater 2022;222:117446. https://doi.org/10.1016/j. actamat 2021 117446
- [54] Sui QX, Wang Z, Wang J, Xu SR, Liu B, Yuan Q, et al. Additive manufacturing of CoCrFeNiMo eutectic high entropy alloy: microstructure and mechanical properties. J Alloys Compd 2022;913:165239. https://doi.org/10.1016/j. iallcom.2022.165239.
- [55] Qiu Y, Xin RS, Luo JB, Ma QX. Effect of deformation modes and heat treatment on microstructure and impact property restoration of internal crack healing in SA 508 steel. Mater Sci Eng, A 2020;778:139073. https://doi.org/10.1016/j. msea 2020.139073
- [56] Pan RC, Fan D, Bian YL, Zhao XJ, Zhang NB, Lu L, et al. Effect of minor elements Al and Ti on dynamic deformation and fracture of CoCrNi-based medium-entropy alloys. Mater Sci Eng. A 2023;884:145535. https://doi.org/10.1016/j.msea.2023.145535.
- [57] Ren C, Sun K, Jia YF, Zhang NZ, Jia YD, Wang G. Effect of Mo addition on the microstructural evolution and mechanical properties of Fe-Ni-Cr-Mn-Al-Ti high entropy. alloys 2023;864:144579. https://doi.org/10.1016/j.msea.2023.144579.
- [58] Liu SY, Wang H, Zhang JY, Zhang H, Xue H, Liu G, et al. Trifunctional Laves precipitates enabling dual-hierarchical FeCrAl alloys ultra-strong and ductile. Int J Plast 2022;159:103438. https://doi.org/10.1016/j.ijplas.2022.103438.
- [59] Lin K, Yu CY, Jiang SH, Cao YL, Li Q, Chen J, et al. High performance and low thermal expansion in Er-Fe-V-Mo dual-phase alloys. Acta Mater 2020;198:271–80. https://doi.org/10.1016/j.actamat.2020.08.012.
- [60] Park JM, Choe J, Kim JG, Bae JW, Moon J, Yang SS. Superior tensile properties of 1%C-CoCrFeMnNi high-entropy alloy additively manufactured by selective laser melting. Mater. Res. Lett. 2020;8(1):1–7. https://doi.org/10.1080/ 21663831 2019 1638844
- [61] Chew Y, Bi GJ, Zhu ZG, Ng FL, Weng F, Liu SB, et al. Microstructure and enhanced strength of laser aided additive manufactured CoCrFeNiMn high entropy alloy. Mater Sci Eng, A 2019;744:137–44. https://doi.org/10.1016/j.msea.2018.12.005.
- [62] Zhu ZG, An XH, Lu WJ, Li ZM, Ng FL, Liao XZ, et al. Selective laser melting enabling the hierarchically heterogeneous microstructure and excellent mechanical properties in an interstitial solute strengthened high entropy alloy. Mater. Res. Lett. 2019;7(11):453–9. https://doi.org/10.1080/ 21663831.2019.1650131.
- [63] Dodd B, Bai YL. Adiabatic shear localization: frontiers and advances. second ed. Amsterdam: Elsevier; 2012.
- [64] Smith TR, Sugar JD, Marchi CS, Schoenung JM. Strengthening mechanisms in directed energy deposited austenitic stainless steel. Acta Mater 2019;164:728–40. https://doi.org/10.1016/j.actamat.2018.11.021.
- [65] Naeem M, He HY, Harjo S, Kawasaki T, Zhang F, Wang B, et al. Extremely high dislocation density and deformation pathway of CrMnFeCoNi high entropy alloy at ultralow temperature. Scripta Mater 2020;188:21–5. https://doi.org/10.1016/j. scriptamat.2020.07.004.
- [66] Williamson GK, Smallman III RE. Dislocation densities in some annealed and coldworked metals from measurements on the X-ray debye-scherrer spectrum. Philos Mag 1956;1(1):34–46. https://doi.org/10.1080/1478643560823807466.
- [67] Schroders S, Sandlobes S, Brike C, Loeck M, Peters L, Tromas C, et al. Room temperature deformation in the Fe₇Mo₆ μ-Phase. Int J Plast 2018;108:125–43. https://doi.org/10.1016/j.iiplas.2018.05.002.
- [68] Liu RY, Wang C, Liu B, Liu Y, Liaw PK, Wang BF. Microstructure and formation mechanisms of nanotwins in the shear band in a FeCoNiCrMo_{0.2} high-entropy alloy. J Mater Res Technol 2022;20:2719–33. https://doi.org/10.1016/j. imrt.2022.08.054.